

# A New Moment Method for Continuum Radiative Transfer in Cosmological Reionization

Kristian Finlator, Feryal Özel, & Romeel Davé

4 November 2021

## ABSTRACT

We introduce a new code for computing time-dependent continuum radiative transfer and non-equilibrium ionization states in static density fields with periodic boundaries. Our code solves the moments of the radiative transfer equation, closed by an Eddington tensor computed using a long characteristics method. We show that pure (i.e., not source-centered) short characteristics and the optically-thin approximation are inappropriate for computing Eddington factors for the problem of cosmological reionization. We evolve the non-equilibrium ionization field via an efficient and accurate (errors  $< 1\%$ ) technique that switches between fully implicit or explicit finite-differencing depending on whether the local timescales are long or short compared to the timestep. We tailor our code for the problem of cosmological reionization. In tests, the code conserves photons, accurately treats cosmological effects, and reproduces analytic Strömgren sphere solutions. Its chief weakness is that the computation time for the long characteristics calculation scales relatively poorly compared to other techniques ( $t_{\text{LC}} \propto N_{\text{cells}}^{1.5}$ ); however, we mitigate this by only recomputing the Eddington tensor when the radiation field changes substantially. Our technique makes almost no physical approximations, so it provides a way to benchmark faster but more approximate techniques. It can readily be extended to evolve multiple frequencies, though we do not do so here. Finally, we note that our method is generally applicable to any problem involving the transfer of continuum radiation through a periodic volume.

**Key words:** radiation transfer — cosmology: theory – early Universe — diffuse radiation — intergalactic medium

## 1 INTRODUCTION

The epoch of reionization is the current frontier in understanding how galaxies form and evolve over cosmic time. After the Universe cooled sufficiently to recombine hydrogen atoms at redshift  $z \approx 1088$  (Spergel et al. 2007), the Universe was fully neutral. Gravity grew ever-denser structures that, at  $z \sim 30 - 50$ , were able to collapse into stars and/or black holes. The radiation emitted from these first objects then began to re-ionize hydrogen. By  $z \sim 6$ , hydrogen reionization appears to be complete (Fan 2007), and the diffuse intergalactic medium (IGM) has a neutral fraction of  $\sim 10^{-4}$ . Understanding this transition epoch is central to understanding the origin of galaxies and the evolution of the IGM. It is a major science driver for a host of upcoming international telescope facilities, such as the *James Webb Space Telescope* and the *Atacama Large Millimeter Array*.

Reionization involves a complex interplay between nonlinear growth of structure, radiative cooling, star/black hole formation, chemical enrichment, and photon transport. Numerical simulations are required to accurately model these highly nonlinear processes. However, the large dynamic range and complex physics involved make this an extraordinarily challenging computational problem. To obtain a full picture of reionization in the context of currently-favored hierarchical structure formation models, it is imperative that simulations include processes of star formation, galaxy formation, and IGM evolution, along with feedback processes that connect all three. Cosmological hydrodynamic simulations accounting for these processes are now achieving maturity, thanks to improving algorithms and computing power. However, the inclusion of radiation transport complicates matters immensely. A cosmological radiative hydrodynamics code that can accurately evolve a representative volume with sufficient dynamic range to study how galaxies reionize the Universe would be a major development towards understanding reionization. In this paper we provide a step towards that end by introducing a new accurate moment-based method for calculating radiative transfer (RT) in a cosmological context.

Time-dependent radiative transfer is one of the most difficult components to treat in any theoretical study of the reionization epoch owing to the problem’s well-known high dimensionality. Consequently, over the past decade, a number of

arXiv:0808.3578v1 [astro-ph] 26 Aug 2008

approximate treatments have emerged that seek to render it more tractable through well-motivated physical approximations. The most flexible methods are the fully analytic treatments (for example, Madau et al. 1999; Wyithe & Loeb 2003; Furlanetto et al. 2004; Iliev et al. 2005; Kramer et al. 2006). These generally involve assuming values for quantities such as the gas clumping factor and the recombination rate that are averaged over all space or, in the case of the excursion-set formalism (Furlanetto et al. 2004), over the volume of an ionized region. In exchange, they readily allow for broad surveys of parameter space to be performed.

The next step in the direction of a full solution is taken by the semi-numerical methods (Ciardi et al. 2000; Mesinger & Furlanetto 2007; Geil & Wyithe 2008; Choudhury et al. 2008), which combine numerically-generated density fields with analytic treatments for radiative transfer using techniques such as the excursion-set formalism in order to account more realistically for source bias and the effects of inhomogeneous density fields. These treatments offer a dramatic increase in realism over purely analytic calculations at modest additional computational cost. However, they have some difficulty accounting fully for the consequences of inhomogeneous density fields such as shadowing and the tendency for low-density regions to have a lower neutral fraction during the later stages of reionization (Choudhury et al. 2008). These problems arise from the need of semi-numerical models to make assumptions regarding the shape of the ionized regions surrounding individual sources and the nontrivial relationship between dark matter and gas densities in the nonlinear regime.

Some of these difficulties are avoided in models that actually solve the radiative transfer equation on numerically-generated density fields but without fully accounting for radiative feedback on the sources (Ciardi et al. 2001; Sokasian et al. 2001; Mellema et al. 2006; McQuinn et al. 2007; Iliev et al. 2007a; see also Iliev et al. 2006 for a very useful comparison of a number of techniques). Nonetheless, obtaining realistic baryonic density and emissivity fields in such contexts still presents considerable challenges (McQuinn et al. 2007). Additionally, while parametrized treatments for radiative feedback have been introduced in such models in order to study, for example, whether the photoevaporation of minihaloes extends the epoch of reionization (Iliev et al. 2007a; McQuinn et al. 2007), the simplified nature of these studies leaves their results open to question (Mesinger & Furlanetto 2007). Hence, while each of these methods has yielded an abundance of insight into reionization and warrant continued development, the need is emerging for a complete solution to the radiative transfer equation that is merged self-consistently with hydrodynamical calculations.

A few fully radiative-hydrodynamic codes have been used to study the reionization epoch (Gnedin & Abel 2001; Cen 2002; Rijkhorst et al. 2006). Unfortunately, the techniques that these codes have introduced do not yet enjoy widespread use owing to their high computational expense, even though such studies are crucial for tuning the assumptions employed in more simplified treatments and verifying their conclusions. Moreover, despite the enormous gain in realism that these codes have afforded the reionization community, they too involve some physical approximations such as the use of the “optically thin variable Eddington tensor” approximation (Gnedin & Abel 2001) and a reduced (Gnedin & Abel 2001) or an infinite speed of light (Cen 2002; Rijkhorst et al. 2006).

In this work, we present a moment method solution to the radiative transfer equation (Auer & Mihalas 1970) and test it on static density fields. Our technique is highly flexible, involves a minimum of physical approximations, and can readily be combined with existing hydrodynamical calculations. It is similar to the method presented by Stone et al. (1992), but with several differences. First, we optimize our code only for cubical simulation volumes with periodic boundaries, as this is typical of cosmological simulations. Second, we derive our Eddington tensors from a long characteristics (LC) calculation in order to minimize artifacts owing to poor angular and spatial resolution. Finally, we include a treatment for nonequilibrium ionizations and account for the cosmological terms in the radiative transfer equation. In a follow-up paper, we will present its implementation within a cosmological galaxy formation code.

We begin in Section 2 by casting the radiative transfer equation into the form in which we solve it and summarizing our numerical method. In Section 3, we compare the performance of long characteristics versus two other time-independent radiative transfer techniques in order to select a method for deriving the Eddington tensor, which we need in order to close our moment hierarchy. After demonstrating that long characteristics introduces the fewest unphysical artifacts, we optimize it for computing reionization using a suite of realistic albeit low-resolution integrations. In Section 4, we discuss our technique for evolving the nonequilibrium ionization field. In Section 5, we summarize our iterative scheme for weaving these ingredients into a self-consistent calculation. In Section 6, we subject our code to a number of standard tests. Finally, we summarize our method and results in Section 7.

## 2 SOLVING THE RADIATIVE TRANSFER EQUATION

We begin this section by writing down the RT equation in comoving coordinates including emission, absorption, and cosmological effects. Next, we recast the RT equation in the form that our code computes and discuss our treatment of the various terms. Finally, we discuss our approach to solving these equations numerically.

### 2.1 The Moments of the Radiative Transfer Equation

The radiative transfer equation in comoving coordinates is (for a derivation, see Gnedin & Ostriker 1997)

$$\frac{1}{c} \frac{\partial \mathcal{N}_\nu(\hat{n})}{\partial t} + \frac{\hat{n}}{a} \cdot \vec{\nabla}_c \mathcal{N}_\nu(\hat{n}) + H \left( 2\mathcal{N}_\nu - \nu \frac{\partial \mathcal{N}_\nu}{\partial \nu} \right) = c\eta_\nu - c\chi_\nu \mathcal{N}_\nu(\hat{n}). \quad (1)$$

Here,  $\mathcal{N}_\nu(\hat{n})$  represents the number of photons with frequency between  $\nu$  and  $\nu + d\nu$  crossing an area  $dA$  in the direction  $\hat{n}$  into a solid angle  $d\Omega$  during a time interval  $dt$ ;  $H$  is the Hubble constant;  $a$  is the cosmological expansion factor;  $\vec{\nabla}_c$  denotes a gradient in comoving coordinates,  $\eta_\nu$  is the local number of photons emitted per unit time per unit solid angle with frequency between  $\nu$  and  $\nu + d\nu$ ;  $c$  is the speed of light; and the absorption mean opacity  $\chi_\nu = \sum_i n_i \sigma_{\nu,i}$  is the sum of the opacities due to the various absorbing species. All emissivities and opacities are taken as isotropic because Equation 1 is written in the cosmological comoving frame. Here and throughout our work, we compute the radiation field in terms of photon number densities rather than energy densities. For simplicity of notation, we will generally omit the  $\hat{n}$ -dependence of  $\mathcal{N}_\nu$  from now on.

The left hand side of Equation 1 is the convective derivative of the photon phase space density but written in terms of  $\mathcal{N}_\nu$ . The first two terms are the classical convective derivative modified to apply in comoving spatial coordinates, and the terms proportional to the Hubble constant account for, respectively, the dilution of  $\mathcal{N}_\nu$  and redshifting of the photon frequencies owing to cosmological expansion. The terms on the right hand side account for photon emission and absorption, respectively.

By integrating over the frequency range  $(\nu_1, \nu_2)$ , we recast Equation 1 in a form appropriate for a multigroup method:

$$\frac{1}{c} \frac{\partial \mathcal{N}}{\partial t} + \frac{\hat{n}}{a} \cdot \vec{\nabla}_c \mathcal{N} = \eta - (\chi_H + \chi_{\text{abs}}) \mathcal{N} \quad (2)$$

Here, we have defined the photon number density  $\mathcal{N}$ , the emissivity  $\eta$ , the cosmological opacity  $\chi_H$ , the spectral slope  $\langle \nu \frac{\partial}{\partial \nu} \rangle$ , and the absorption mean opacity  $\chi_{\text{abs}}$  as follows:

$$\mathcal{N} \equiv \int_{\nu_1}^{\nu_2} \mathcal{N}_\nu d\nu \quad (3)$$

$$\eta \equiv \int_{\nu_1}^{\nu_2} \eta_\nu d\nu \quad (4)$$

$$\chi_H \equiv \frac{H}{c} \left( 2 - \langle \nu \frac{\partial}{\partial \nu} \rangle \right) \quad (5)$$

$$\langle \nu \frac{\partial}{\partial \nu} \rangle \equiv \int_{\nu_1}^{\nu_2} \nu \frac{\partial \mathcal{N}_\nu}{\partial \nu} d\nu / \int_{\nu_1}^{\nu_2} \mathcal{N}_\nu d\nu \quad (6)$$

$$\chi_{\text{abs}} \equiv \int_{\nu_1}^{\nu_2} \chi_\nu \mathcal{N}_\nu d\nu / \int_{\nu_1}^{\nu_2} \mathcal{N}_\nu d\nu. \quad (7)$$

Equation 2 is equivalent to an integral of Equation 1 over frequency as long as the frequency-averaged cosmological and absorption mean opacities  $\chi_H$  and  $\chi_{\text{abs}}$  can be determined consistently. Both depend on the slope of the spectrum at each frequency bin. The dependence of the absorption mean opacity  $\chi_{\text{abs}}$  is clear, and the dependence of the cosmological opacity  $\chi_H$  can be made more intuitive by noting that, for a power-law spectrum  $\mathcal{N}_\nu \propto \nu^{-\alpha}$ , the spectral slope  $\langle \nu \frac{\partial}{\partial \nu} \rangle$  is given by  $-\alpha$ . In this case, the cosmological opacity  $\chi_H$  reduces to  $\frac{H}{c}(2 + \alpha)$ . This term is generically quite small in the problem of cosmological reionization: For star-forming galaxies and active galactic nuclei, the slope of the ultraviolet continuum generally falls within the range  $\alpha \sim 0.3$ – $5$ , so during the reionization epoch  $\chi_H \sim 0.1$ – $3 \times 10^{-26} \text{ cm}^{-1}$ . By contrast, even for a neutral hydrogen fraction of  $10^{-3}$  at  $z = 6$  (Fan et al. 2006), the opacity at  $912\text{\AA}$  at the mean density is around  $3$ – $4 \times 10^{-25} \text{ cm}^{-1}$ . This is simply a statement that, throughout the reionization epoch, ionizing photons tend to be absorbed long before they can be diluted or redshifted by the Hubble flow. For this reason, we bring the cosmological term to the right-hand side of Equation 2. In multifrequency computations we will allow the spectral slope  $\alpha$  to vary self-consistently with frequency by using the value from the previous timestep. However, in the present work, we neglect it entirely as we consider only monochromatic problems. From now on, we use the opacity  $\chi$  to refer to the sum of the cosmological and absorption mean opacities:  $\chi \equiv \chi_H + \chi_{\text{abs}}$ .

The first two angle moments of Equation 2 are:

$$\frac{\partial \mathcal{J}}{\partial t} = -\frac{1}{a} \vec{\nabla}_c \cdot \vec{\mathcal{F}} + 4\pi\eta - c\chi\mathcal{J} \quad (8)$$

$$\frac{\partial \vec{\mathcal{F}}}{\partial t} = -\frac{c}{a} \vec{\nabla}_c \cdot (c\mathbf{f}\mathcal{J}) - c\chi\vec{\mathcal{F}} \quad (9)$$

$$\mathbf{f} \equiv \frac{\int \mathcal{N} \hat{n} \hat{n} d\Omega}{\int \mathcal{N} d\Omega}. \quad (10)$$

The zeroth and first moments  $\mathcal{J}$  and  $\vec{\mathcal{F}}$  are the angle-averaged mean number density (hereafter “number density”) and flux of photons in a frequency bin, respectively, and the Eddington tensor  $\mathbf{f}$  is used to close the moment hierarchy; we will discuss how we obtain the Eddington tensor in Section 3.

When constructing a solution to equations 8 and 9, it is important to center the photon number density, flux, and the components of the Eddington tensor about each cell spatially in such a way that the resulting finite-difference approximation for the number density at the updated time (Equation 11) is cell-centered. This is important not only to improve the solution’s accuracy in space, but also because improper centering can lead to spurious anisotropies in the radiation field or even prevent the solution from converging altogether. Accordingly, we center the variables as follows:  $\mathcal{J}$  and diagonal components of  $\mathbf{f}$  are positioned at the cell center, components of  $\vec{\mathcal{F}}$  are stored at cell faces, and off-diagonal elements of  $\mathbf{f}$  are stored at cell edges (see Figure 1).

One ambiguity remains regarding the treatment of off-diagonal elements of  $\mathbf{f}$  such as  $\mathbf{f}_{\mathbf{x}\mathbf{y}} \equiv \int \mathcal{N} \hat{x} \hat{y} d\Omega / \int \mathcal{N} d\Omega$ . Proper

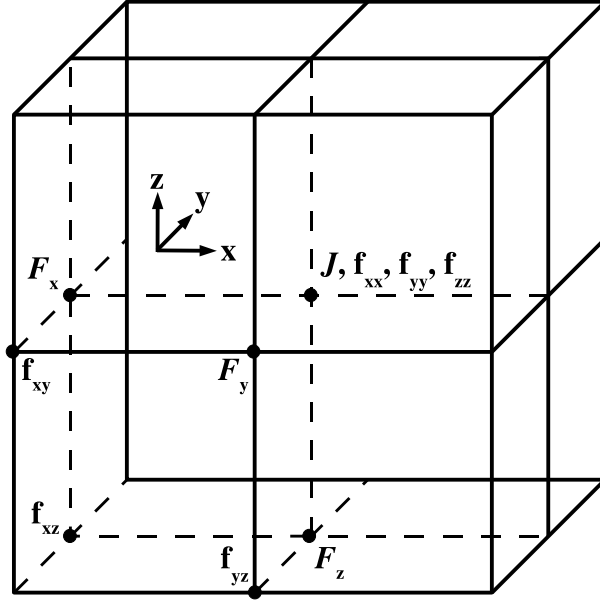


**Figure 1.** The centering scheme for our radiative variables.

centering requires that these factors always enter into the partial derivatives of Equation 13 via a spatially-averaged product with the photon number density  $\mathcal{J}$ . For example, the finite-difference approximation for  $\mathcal{J}^{n+1}(i, j, k)$  includes, among other things, the spatial average of the product  $\mathbf{f}_{xy}\mathcal{J}$  over the cells  $(i, j, k)$ ,  $(i-1, j, k)$ ,  $(i, j-1, k)$ , and  $(i-1, j-1, k)$ . In such instances, it is possible to use either the “average of the products”,  $\langle \mathbf{f}\mathcal{J} \rangle$  or the “product of the averages”,  $\langle \mathbf{f} \rangle \langle \mathcal{J} \rangle$ . Testing suggests that the differences between the two options are small, but inspection shows that the “average of the products” option gives rise to significant cancelling of terms within the full finite-difference expression and hence could lead to less smooth solutions. For this reason, we prefer the “product of the averages” approach.

## 2.2 Solving the Radiation Transfer Equation

We now discuss our technique for integrating Equations 8 and 9 numerically. These equations can be quite stiff when applied to the problem of cosmological reionization, hence we use an implicit finite-differencing scheme in time. In other words, we use the photon number density and flux at the updated time on the right hand side of Equations 8 and 9. SMN92 solved the resulting system using the “Automatic Flux-Limiting” prescription of Mihalas & Weaver (1982). This scheme proceeds by integrating Equation 9 over one timestep analytically before plugging the result into an implicitly finite-differenced form of Equation 8. However, Hayes & Norman (2003) found that the results from this technique do not differ significantly from the results of simply finite-differencing Equation 9. Our own testing also indicates that the latter technique produces accurate results, hence in our code the updated flux  $\vec{\mathcal{F}}^{n+1}$  and number density  $\mathcal{J}^{n+1}$  relate to the previous values  $\vec{\mathcal{F}}^n$  and  $\mathcal{J}^n$  as follows:

$$\mathcal{J}^{n+1} = \frac{1}{1+x^{n+1}} \left[ \mathcal{J}^n + 4\pi\eta\Delta t - \Delta t \frac{\vec{\nabla}_c}{a} \cdot \left( \frac{\vec{\mathcal{F}}^n}{1+x^{n+1}} \right) + c^2 \Delta t^2 \frac{\vec{\nabla}_c}{a} \cdot \left[ \frac{1}{1+x^{n+1}} \frac{\vec{\nabla}_c}{a} \cdot (\mathbf{f}\mathcal{J}^{n+1}) \right] \right] \quad (11)$$

$$\vec{\mathcal{F}}^{n+1} = \frac{1}{1+x^{n+1}} \left[ \vec{\mathcal{F}}^n - c^2 \Delta t \frac{\vec{\nabla}_c}{a} \cdot (\mathbf{f}\mathcal{J}^{n+1}) \right] \quad (12)$$

$$x^{n+1} \equiv c\chi^{n+1}\Delta t$$

These equations can be combined and rearranged into the form

$$\mathbf{A} \cdot \vec{\mathcal{J}}^{n+1} = \vec{b}, \quad (13)$$

where the vector notation indicates that we are solving a coupled system of algebraic equations with dimension equal to the number of computational cells. The update matrix  $\mathbf{A}$  is a function of  $\vec{\mathcal{J}}^n$  and  $\vec{\mathcal{F}}^n$  but not  $\vec{\mathcal{J}}^{n+1}$ , hence the photon number densities may be updated via a simple matrix inversion. The photon number density in each cell couples only to 18 of its neighboring cells. Consequently, only 19 elements in each row of  $\mathbf{A}$  are nonzero, making it a sparse matrix.

Linear systems of equations for which the coefficient matrix is sparse but not both symmetric and positive definite can be solved via the biconjugate gradient method. We have found that the preconditioned biconjugate gradient routine *linbcg* in

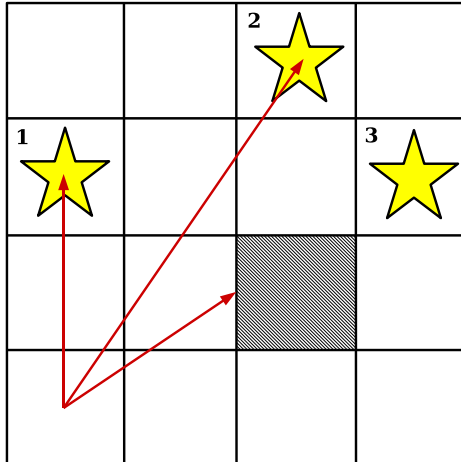


**Figure 2.** A sketch of our long characteristics method in two dimensions. Long characteristics from the bottom-left cell to sources 1 and 2 are shown; the line integral to source 3 is halted when it encounters an intervening optically thick cell.

*Numerical Recipes* (Press et al. 1992) solves the problem rapidly. We use the diagonal of  $\mathbf{A}$  as the preconditioner and halt the iteration when the residual  $|\mathbf{A} \cdot \vec{\mathcal{J}}^{n+1} - \vec{b}|/|\vec{b}|$  is less than  $10^{-6}$ .

We generalize this technique to multifrequency problems by solving Equations 11 and 12 independently for a number of multigroup frequency bins. We compute the Eddington tensor  $\mathbf{f}$ , absorption mean opacity, and cosmological opacity fields separately for each frequency bin. When evaluating Equations 5–7, we use the spectrum  $\mathcal{J}(\nu)$  from the previous timestep.

### 3 COMPUTING THE EDDINGTON FACTORS

As is well-known, the primary difficulty in solving the radiative transfer equation lies in its high dimensionality. Treating the moments of the equation does not suppress this dimensionality unless the photon mean free path is short compared to all length scales of interest, in which case one can close the moment hierarchy with analytical flux-limiters (e.g., Hayes et al. 2006). This is not the case in the problem of cosmological reionization, hence an accurate solution depends critically on an accurate derivation of the Eddington tensor  $\mathbf{f}$ . This in turn requires knowing how the photon density  $\mathcal{N}$  varies as a function of direction  $\hat{n}$  (see Equation 10). A fully consistent treatment would obtain  $\mathcal{N}(\hat{n})$  via a time-dependent integration of the radiative transfer equation; however, if this were easily done then of course the entire problem would already be solved. Here, we derive the Eddington tensor  $\mathbf{f}$  from a time-independent formal solution to the radiative transfer equation (that is, a solution in which  $\partial\mathcal{N}_\nu/\partial t = 0$ ; see also Auer & Mihalas 1970; SMN92). We note that this is our only approximation.

Previous efforts have approached this problem through computationally *efficient* techniques such as short characteristics (Stone et al. 1992; Hayes & Norman 2003) or the optically thin approximation (Gnedin & Abel 2001). While these techniques have their strengths and have led to a great deal of insight into reionization, the associated compromises in accuracy are poorly-understood. For this reason, we undertake an *accurate* calculation of the Eddington tensor, even though this degrades our computational efficiency, in order to study its impact on cosmological problems. In this section, we begin by reviewing the long characteristics (LC) technique for computing the Eddington tensor  $\mathbf{f}$ . We then compare it to SC and the optically thin approximation in order to highlight the strengths of LC. Finally, we optimize LC for calculations of cosmological reionization.

#### 3.1 Long Characteristics

The LC approach to computing  $\mathcal{N}(\hat{n})$  at a target cell consists of integrating the (time-independent) radiative transfer equation along characteristics that run in the directions  $\hat{n}_i$  from the target cell to the source cells  $i$ . The photon density at the target cell is then given by the sum

$$\mathcal{N}(\hat{n}) = \sum_i \frac{\eta_i}{\chi_i} e^{-\tau_i} \delta(\hat{n} - \hat{n}_i), \quad (14)$$

where the index  $i$  runs over all source cells and  $\tau_i$  is the total optical depth between the target cell and the source cell  $i$ . The problem of computing  $\mathcal{N}(\hat{n})$  at a target cell hence reduces to one of determining the total optical depth  $\tau_i$  to each source cell. Here, we outline our approach to computing  $\tau_i$  (see also Figure 2). We note that our treatment is similar to the ray-tracing technique of Abel et al. (1999).

Consider the contribution to the Eddington tensor in a target cell whose center is located at  $\vec{r}_T \equiv (x_T, y_T, z_T)$  owing to a source cell  $i$  whose center is located at  $\vec{r}_i \equiv (x_i, y_i, z_i)$ . We compute the optical depth between the two cells by integrating

along a ray that points in the direction  $\hat{n} = (n_x, n_y, n_z) = (\vec{r}_i - \vec{r}_T) / |\vec{r}_i - \vec{r}_T|$ . Starting at  $\vec{r}_T$ , the distance in the direction  $\hat{n}$  to the nearest  $y$ - $z$  plane  $\Delta r_x$  is given by

$$\Delta r_x = \left[ \frac{\Delta x}{2} - \text{sign}(n_x)(x - x_c) \right] \sqrt{1 + \left(\frac{n_y}{n_x}\right)^2 + \left(\frac{n_z}{n_x}\right)^2}, \quad (15)$$

where  $\text{sign}(x)$  equals  $-1$  or  $+1$  if  $x$  is negative or positive, respectively. Analogous relations exist for the distance to the next  $x$ - $z$  boundary  $\Delta r_y$  and the next  $x$ - $y$  boundary  $\Delta r_z$ . We determine which cell the ray enters next by evaluating which of the three distances is shortest; for example, if  $\Delta r_x < \Delta r_y$  and  $\Delta r_x < \Delta r_z$ , then the ray will next encounter a  $y$ - $z$  plane. We then add the contribution  $\chi \Delta r$  to the optical depth from the cell that the ray just traversed assuming that  $\chi$  is uniform throughout the cell. Repeating this procedure, we continue adding contributions to the line integral until either the ray enters the source cell or the accumulated optical depth exceeds a maximum value  $\tau_{\text{max}}$  that will be determined from convergence testing. If the accumulated optical depth exceeds  $\tau_{\text{max}}$  before the ray enters the source cell  $i$ , then we consider the source to be completely obscured and halt the line integral. Otherwise, we add the contribution of the source cell to the Eddington tensor at the target cell and proceed to the next source cell.

If the cell is itself a source, then we account for the contribution of its self-illumination to its Eddington tensor  $\mathbf{f}$  by adding  $(4\pi\mathcal{N}_0/3)\mathbf{1}$  to the numerator and  $4\pi\mathcal{N}_0$  to the denominator in Equation 10, where  $\mathbf{1}$  indicates the unit tensor and  $\mathcal{N}_0$  is given by

$$\begin{aligned} \mathcal{N}_0 &= \frac{\eta}{\chi}(1 - e^{-\chi r_*}) \\ r_* &= \left( \frac{\Delta x \Delta y \Delta z}{\frac{4}{3}\pi} \right)^{\frac{1}{3}}. \end{aligned}$$

## 3.2 Comparison of Techniques

### 3.2.1 Short Characteristics

The method of short characteristics (SC) has been introduced elsewhere (Kunasz & Auer 1988; Stone et al. 1992) and we will only summarize it here. The SC approach involves solving the radiative transfer equation within each cell along characteristics that run from the cell's faces to its center using boundary conditions at the cell faces that are obtained through interpolation. Given the boundary conditions on the computational volume, one simply marches downstream from one side of the volume to the other so that, at each cell, the upstream boundary conditions are always known. As long as the opacity and emissivity do not change dramatically on the scale of a computational cell and some spatial diffusion of the radiation field is acceptable, SC is an efficient technique for computing a time-independent formal solution to the RT equation (or even a time-dependent one; see Hayes & Norman (2003)): In three dimensions, the computation time scales with the number of cells on each side of the computational grid  $n_{\text{grid}}$  as  $O(n_{\text{grid}}^3)$ . Unfortunately, if the emissivity or opacity varies significantly on the scale of the computational grid, then the interpolations can give rise to dramatic numerical artifacts in the spatial distribution of the photon number density. In the problem of cosmological reionization, sources are generally pointlike and there are sharp transitions between optically thick and thin regions (for example, at ionization fronts), hence such artifacts are expected. Additionally, given that the emissivity is highly concentrated spatially, the number of angles that must be sampled in order to yield smooth ionization fronts can scale as poorly as  $O(n_{\text{grid}}^2)$ , yielding a less-favorable overall scaling of  $O(n_{\text{grid}}^5)$  (see, for example, Razoumov & Scott 1999).

The tendency for collimated radiation fields to diffuse numerically in SC owing to the interpolated boundary conditions at each cell has been discussed elsewhere (for example, Kunasz & Auer 1988). However, the anisotropies that can also result from these interpolations have not received much attention. In order to demonstrate this problem, we consider the idealized case of a galaxy consisting of  $10^8 M_\odot$  of young stars at  $z = 20$  with an ionizing escape fraction of 10%. We locate the galaxy at the center of a homogeneous region 0.5 (proper) Mpc on a side in which pure hydrogen of total number density  $1.5 \times 10^{-3} \text{ cm}^{-3}$  and temperature  $10^4 \text{ K}$  is ionized to a neutral fraction of  $10^{-3}$ . We solve the time-independent radiative transfer equation for this scenario using both SC and LC. In the SC integration we sample the unit sphere with 320 uniformly-distributed unit vectors. In both cases we use a grid resolution of  $64^3$  cells.

In Figure 3 we show contours of photon number density versus position in a plane that contains the source. The interpolations that are inherent to SC give rise to strong anisotropies in the number density field owing to the discontinuous emissivity field at the source. These can be alleviated (but not eliminated) by significantly increasing spatial and angular resolution, but at the cost of increased computation time. Not surprisingly, tests indicate that using SC-derived Eddington factors to solve the Strömgren Sphere problem within our full time-dependent moments method gives rise to unacceptable anisotropies in the shape of the ionization front. By contrast, LC yields smooth mean intensity contours because it does not involve any interpolations.

We have compared the performance of LC only to simple (that is, not source-centered) SC. A source-centered SC method (for example, Mellema et al. 2006) would probably perform differently although the required interpolations are still likely to lead to numerical artifacts. However, we have opted not to consider source-centered SC here because it is not obvious that the computation time for this variant scales more favorably with spatial resolution than it does for LC.

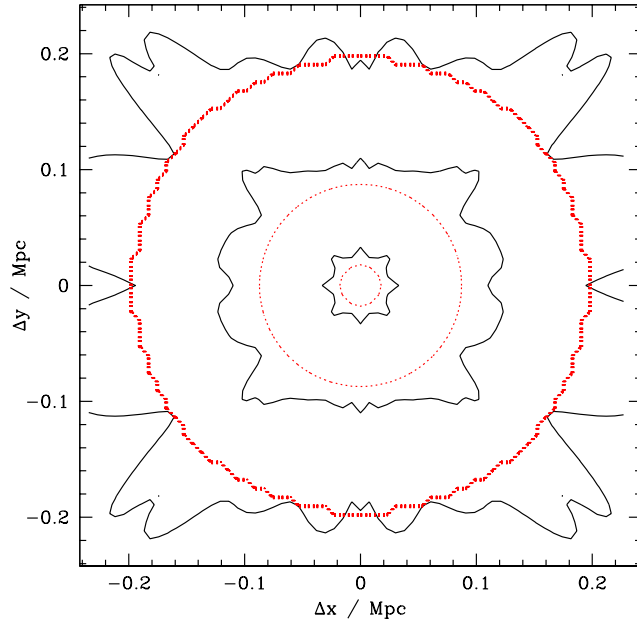


**Figure 3.** Contours in photon number density versus position in a plane that contains the source as calculated using SC (black solid) and LC (red dotted). The strong anisotropies resulting from the interpolations that are inherent to SC compare unfavorably to LC, which does not involve interpolations.

### 3.2.2 Optically Thin Approximation

The optically thin approximation (Gnedin & Abel 2001) involves evaluating Equation 10 via a time-independent formal solution to the radiative transfer equation in which the opacity is neglected. Specifically,  $\mathcal{N}$  is calculated from the sum total of all photons emitted in the volume, with no attenuation. This approach conserves photons, does not suffer from some of the grid-induced artifacts that can occur in the SC approach, and yields results that are qualitatively reasonable. Moreover, the computation time scales as  $O(N^3)$ . These desirable characteristics motivate us to evaluate the benefits of accurately accounting for the optical depth, and the most direct way to do so is simply to compare the results of using optically thin versus accurate Eddington tensors within our moment method. Our LC code is well-suited for performing such a comparison. For this reason, we revisit the problem of multiple sources embedded in an initially optically thick medium. In the optically thin approximation, a source can affect the Eddington tensor in the vicinity of a neighboring source even before their respective H II regions have overlapped. This can potentially lead to errors in the shape of the resulting ionization fronts even before they overlap (see also Gnedin & Abel 2001).

We consider the problem of a bright source with a monochromatic ionizing luminosity of  $5 \times 10^{48} \text{ s}^{-1}$  located 2.2 kpc from a faint source whose luminosity is  $5 \times 10^{47} \text{ s}^{-1}$ . Both sources are embedded in a homogeneous medium of pure hydrogen with number density  $10^{-3} \text{ cm}^{-3}$  and temperature  $10^4 \text{ K}$ . The medium is initially entirely neutral. In this arrangement, the flux from the bright source dominates that of the faint source at a distance from the faint source equal to one quarter of the faint source’s Strömgren radius. We evolve this system with Eddington tensors obtained from LC and the optically thin approximation until the sources’ H II regions overlap at  $t \approx 5 \text{ Myr}$ . We use a grid of  $80^3$  computational cells and disable periodic boundary conditions.

In Figure 4, we compare the resulting neutral fractions along the line passing through the source centers before, during, and after overlap. At  $t = 0.5 \text{ Myr}$ , the two H II regions are evolving approximately correctly in the optically thin approximation although there is a suggestion that photons stream too rapidly along the direction connecting the two sources. By  $t = 1.5 \text{ Myr}$ , there is a noticeable tendency for the ionization fronts to advance too rapidly between the two sources in the optically thin case. This tendency oversuppresses the neutral fraction in this region. By  $t = 2.5 \text{ Myr}$ , it is clear that overlap has occurred too soon in the optically thin approximation. Finally, after overlap has occurred ( $t = 5 \text{ Myr}$ ) the optically thin approximation performs well again because, at least within the ionized region, it is no longer a strong approximation.

In Figure 5, we compare the morphologies of the H II regions at  $t = 2.1 \text{ Myr}$ . The left and right panels show the results of using the optically thin approximation and long characteristics, respectively. Looking at the right panel first, we see that the H II regions show slight departures from spherical symmetry even with accurate Eddington tensors, appearing slightly boxy in this projection owing to low spatial resolution. In addition to this asymmetry, however, the smaller H II region appears dramatically elongated prior to overlap when we use the optically thin approximation to compute the Eddington tensors. In fact, the optically thin approximation causes both H II regions to elongate along the axis that connects the two sources, leading to the early overlap seen in Figure 4.

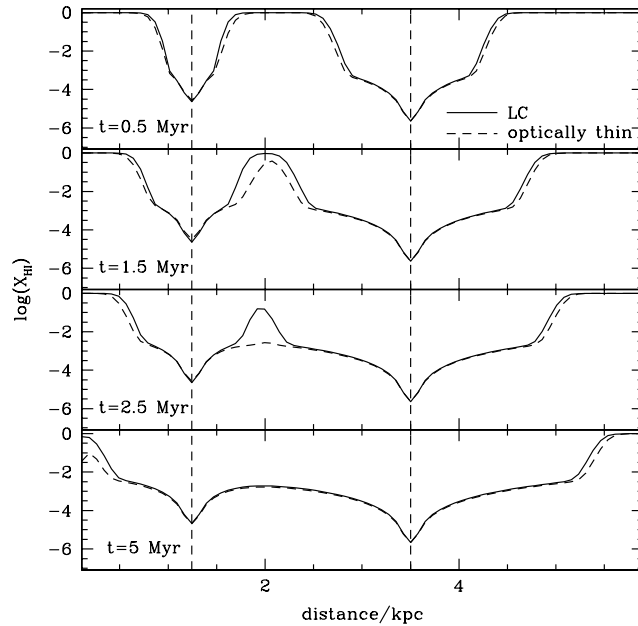


**Figure 4.** Neutral fraction as a function of position along a line connecting a bright source and a faint source at three different times. The solid and dashed curves show the results obtained when computing the Eddington tensor through LC and the optically thin approximation, respectively. The vertical dashed lines indicate the positions of the sources. The optically thin approximation does well at early and late times, but the individual H II regions overlap too quickly and the ionization front from the faint source is too extended during the overlap phase.

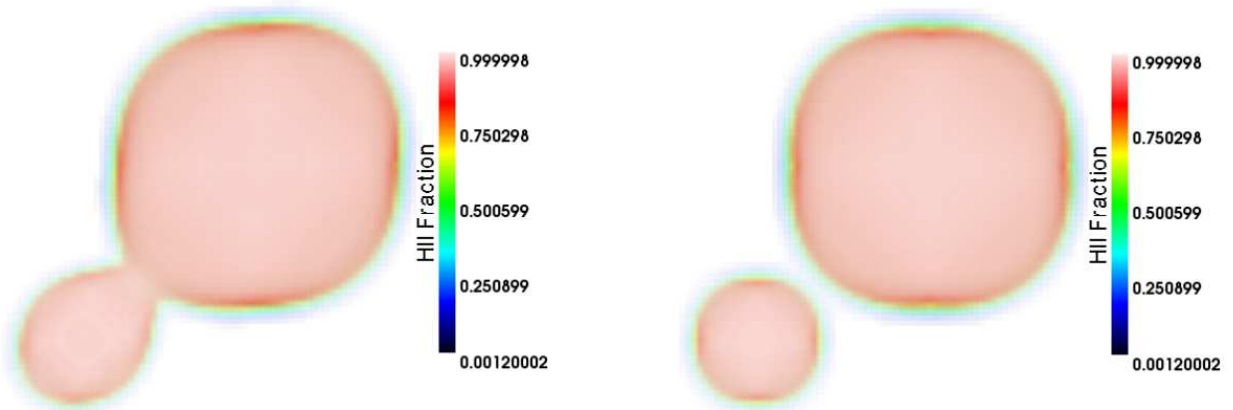


**Figure 5.** Ionized hydrogen fraction as a function of position for the test in Figure 4 at  $t = 2.1$  Myr. The left and right panels show how the H II regions appear when we compute the Eddington tensors using the optically thin approximation and long characteristics, respectively. The smaller H II region is dramatically elongated in the optically thin approximation. These figures were produced using IFRIT.

What effect do morphological errors and a tendency towards early overlap have on galaxy evolution during the recombination epoch? Figures 4 and 5 suggest that the errors will be small on scales that are larger than the largest ionized regions at any given time. The fact that moment methods automatically conserve photons irrespective of the Eddington tensors reinforces this view. However, at smaller scales it is possible that galaxy evolution in satellite halos will be oversuppressed, especially in regions between larger halos. Such an error could in turn lead to an underestimate of the number density of smaller ionized regions, which may dominate the photon budget of overdense regions (Iliev et al. 2007b). The only way to settle this question will be through full-scale simulations of reionization in which the two techniques can be compared.

### 3.3 Optimizing the Long-Characteristics Calculation

Our LC calculation of the Eddington tensors is time consuming. To optimize the calculation, we introduce some numerical approximations. Because these approximations are numerical and not physical, it is possible to rigorously assess the errors introduced through convergence tests. The key optimization is that we only recompute the Eddington tensor field when the radiation field has changed significantly, and not at every timestep of the moment solver. Since in typical cosmological situations the radiation field evolves relatively slowly over much of the volume, this results in many fewer LC calculations. In this section we discuss our optimizations and quantify the errors.

The first problem that we must address in optimizing our LC technique for cosmological reionization is the way that we smooth the Eddington tensor field. Smoothing is necessary because discontinuities in the opacity field (for example, around isolated sources or at ionization fronts) give rise to discontinuities in the Eddington tensor field, which in turn imprint numerical artifacts onto the morphology of the radiation and ionization fields. Moreover, in extreme cases, discontinuities in the Eddington tensors can prevent the code from converging altogether (as also noted by Razoumov & Scott 1999). While the optimal solution to these problems would be to enforce a spatial resolution in which no cell is optically thick, this condition is computationally prohibitive. We have found that smoothing the Eddington tensor field with a 27-cell tophat filter largely removes the numerical effects (see, however, Figure 5). This smoothing does not degrade the quality of our solution for two reasons: (1) it does not impact photon conservation, and (2) it does not reduce the solution’s spatial resolution because the moment method is already second-order in space; that is, we smooth over the same spatial scales to compute the spatial derivatives.

Next, we turn to the choice of numerical parameters. Our implementation of LC introduces three parameters that we optimize through convergence tests: (1) The maximum optical depth from a target cell to a source cell  $\tau_{\max}$  beyond which we consider the source to be obscured and halt its LC line integral; (2) the depth  $n_d$  of periodic replicas that we use to mimic periodic boundaries; and (3) the minimum fractional change in photon number density  $f_{\mathcal{J}}$  required to trigger an update to a cell’s Eddington tensor. Generally, we will require a 10% median accuracy on the photon number density  $\mathcal{J}$ .

Our convergence tests involve computing the reionization of a static cosmological density and emissivity field. We obtain this field by dividing the gas and stellar densities from the  $z = 9$  snapshot of an  $8h^{-1}\text{Mpc}$  cosmological volume (the w8n256vzw simulation of Oppenheimer & Davé 2006) onto a  $16^3$  grid. We divide the total mass associated with SPH particles that lie near cell boundaries between the cells by summing incomplete gamma functions to their equivalent Plummer SPH smoothing kernels. We assume that all gas is completely neutral at  $z = 9$ . We compute the cell emissivities by convolving the stellar populations in each cell with the Bruzual & Charlot (2003) stellar population synthesis models and assuming a 10% escape fraction for ionizing photons. During the integration, we account for cosmological expansion by assuming  $(\Omega, \Lambda, H_0) = (0.3, 0.7, 70)$ . With this setup, we find that the volume-averaged neutral fraction drops to roughly  $x_{\text{HI}} = 10^{-3}$  at  $z = 6$  (Figure 16), in good agreement with available constraints (Fan et al. 2006).

#### 3.3.1 Optimizing the Maximum Optical Depth

We look for an optimal maximum optical depth  $\tau_{\max}$  beyond which the effect of terminating the LC line integrals is small. To do so, we compute the reionization of our cosmological test case assuming  $\tau_{\max} = 1, 5, 6,$  and  $1000$  and using the hybrid treatment for the periodic depth  $n_d$  (see Section 3.3.2). We compare in Figure 6 the resulting errors.

The top panel shows how the median fractional error in the local photon number density  $\mathcal{J}$  varies with integration time, where we compute the fractional errors by comparing against the  $\tau_{\max} = 1000$  test case. At early times ( $\log(x_{\text{HI}}) > -0.5$ ) the fractional errors are small regardless of the choice of  $\tau_{\max}$ . This simply reflects the fact that, at this epoch, reionization is dominated by scales below our spatial resolution so that radiative transfer between cells is subdominant to self-ionization of individual cells. As  $\log(x_{\text{HI}})$  drops below  $-0.5$ , however, the transport of photons between cells becomes more important and the errors in the LC calculation become noticeable. The errors reach a maximum at the point when the individual H II regions begin to overlap ( $\log(x_{\text{HI}}) \sim -1$ ), and then begin to decline slowly as the universe becomes increasingly optically thin. The slow decline in errors at late times owes to the fact that cells can “see” more sources and the Eddington tensors become more nearly isotropic irrespective of  $\tau_{\max}$ . Comparing the error trends for different values of  $\tau_{\max}$ , we find that the accuracy errors seem nearly converged even for  $\tau_{\max} = 1$ .

The bottom panel shows the distribution of accumulated fractional errors in local photon number density at the point where the neutral fraction  $x_{\text{HI}}$  has dropped to 7%. There is a peak in the error distribution near 10-20%, with significant tails out to low errors and a few regions with errors of order unity. We find no correlation between the magnitude and fractional error in  $\mathcal{J}$ ; in other words, bright regions are equally as likely as faint ones to suffer large fractional errors. As in the top panel, the solution seems generally converged even for  $\tau_{\max} = 1$  although the errors for  $\tau_{\max} = 5$  and  $6$  are slightly lower systematically. Evidently, choosing  $\tau_{\max} = 1$  would be sufficient to guarantee a median accuracy better than 10% at all times; however, in order to be conservative, we choose  $\tau_{\max} = 6$ .

#### 3.3.2 Optimizing the Periodic Depth

Hydrodynamical simulations of cosmological volumes assume periodic boundaries. We are thus faced with the problem of accounting for periodic boundaries in our LC calculations. Unfortunately, an analytic treatment is impossible as it cannot be determined a priori whether a cell can “see” a source in a periodic replica of the volume. The only obvious treatment is the

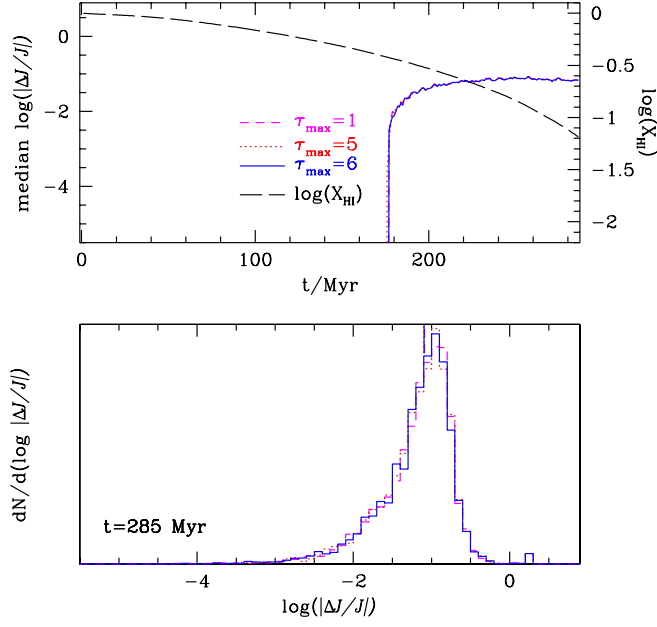


**Figure 6.** Convergence-testing the parameter that controls the optical depth at which LC line integrals are terminated,  $\tau_{\max}$ , by comparing fractional errors in the local photon number density  $\mathcal{J}$  as a function of time. We compute reionization using  $\tau_{\max} = 1$  (short-dashed magenta),  $\tau_{\max} = 5$  (dotted red) and  $\tau_{\max} = 6$ , (solid blue); we obtain the “converged” answer by assuming  $\tau_{\max} = 1000$ . The top panel shows the median local error in  $\mathcal{J}$  as a function of time while the bottom panel shows the full distribution of local fractional errors at  $t = 285$  ( $z = 6.5$ ,  $x_{\text{HI}} = 0.07$ ). The vertical lines at the top of the bottom panel indicate the medians. Here and in Figures 7 and 8, we consider only cells with comoving photon number density  $\mathcal{J} > 1 \times 10^{-10} \text{ cm}^{-3}$  in order to eliminate cells where  $\mathcal{J}$  is dominated by roundoff error. Choosing  $\tau_{\max} = 6$  yields median fractional accuracy errors  $\leq 10\%$  at all times.

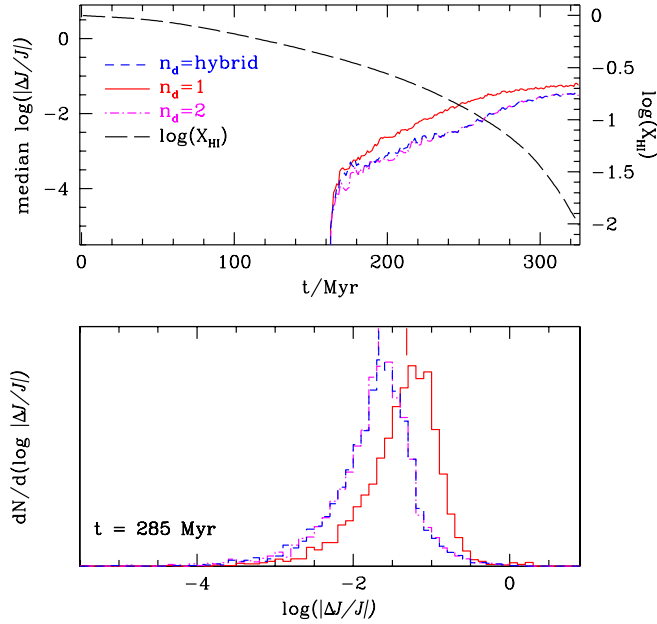


**Figure 7.** Convergence-testing the parameter that controls the number of simulation volume replicas used to mimic periodic boundaries,  $n_d$ , by comparing fractional errors in the local photon number density  $\mathcal{J}$  as a function of time. We compute reionization using  $n_d = 1$  (red solid),  $n_d = 2$ , (magenta dot-dashed), and using a hybrid scheme in which  $n_d$  switches from 1 to 2 when the volume-averaged neutral hydrogen fraction dips below 0.5 (blue short-dashed); the “converged” answer is obtained by assuming  $n_d = 5$ . The meanings of the various curves are analogous to Figure 6. The hybrid scheme yields median fractional accuracy errors of less than 10% at all times.

brute-force approach of mimicking periodic boundaries by positioning periodic replicas around the simulation volume. Each source is then reproduced in each replica, and the LC line integrals must be computed from each cell in the central volume to each copy of each source. We use the periodic depth parameter  $n_d$  to indicate the depth of the periodic replicas. For example,  $n_d = 1$  corresponds to positioning 26 replica volumes about the simulation. Clearly, accuracy and computation time both grow with  $n_d$ . Our problem thus reduces to determining the minimal value of  $n_d$  that allows for better than 10% accuracy at all times.

It is tempting to suppose that, since the universe is optically thick until the neutral fraction  $x_{\text{HI}}$  drops below  $\sim 10^{-3}$ , using  $n_d = 1$  should be adequate until then. However, straightforward testing indicates that this leads to median errors in photon number density that approach 10% even when  $x_{\text{HI}} > 5\%$ . In order to determine what value of  $n_d$  leads to converged behavior, we have computed the reionization of a static density field from  $z = 9 \rightarrow 6$  using  $n_d = 1, 2, 5$ . We also introduce a hybrid scheme in which  $n_d$  changes from 1 to 2 when the mean neutral fraction drops below 0.5, which, as we will show, is the best alternative.

In Figure 7, we show how the resulting fractional errors vary with time. The top panel shows the median fractional error in local photon number density as a function of time. We compute the fractional error by comparing with the  $n_d = 5$  result, which yields a very nearly converged solution for low neutral fractions and completely converged solutions for  $x_{\text{HI}} > 50\%$ . At early times ( $x_{\text{HI}} > 0.6$ ), the universe is so optically thick that few cells are affected by sources in replica volumes. In this regime, using  $n_d = 1$  leads to negligible errors. As  $x_{\text{HI}}$  approaches 0.5, however, some of the H II regions grow to substantial fractions of the simulation volume and cross its boundaries so that the median fractional error begins to rise. By the time  $x_{\text{HI}} = 0.01$  ( $z \approx 6.3$ ), the median fractional error exceeds 1% even if  $n_d = 2$ . Not surprisingly, the errors from  $n_d = 1$  are larger at all timesteps.

The bottom panel shows the distribution of accumulated fractional errors in local photon number density at the point where the neutral fraction has dropped to 7%. There is a peak in the error distribution near 5–10%, with significant tails out to low errors and a few regions with fractional errors of order unity. The errors in the hybrid scheme are comparable to the errors for  $n_d = 2$ , with a median error of 3%. Noting that the errors generally increase with timestep, we conclude that the hybrid scheme leads to median errors that are always  $\leq 10\%$ .

The hybrid  $n_d$  scheme speeds up our code significantly. We have verified through direct testing that the LC computation time varies with the periodic depth roughly as  $(2n_d + 1)^3$  (that is, proportional to the total number of volumes), regardless of both the spatial resolution and the ionization state of the universe. It follows that, for a calculation in which  $x_{\text{HI}}$  drops below 50% after roughly half of the total integration time has elapsed, using hybrid  $n_d$  rather than using  $n_d = 2$  reduces the computation time by up to  $\approx 40\%$  without affecting the accuracy. Hence this is the preferred option.

### 3.3.3 Optimizing the Eddington Tensor Update Criterion

Our technique involves periodically updating the Eddington tensor field in order to maintain consistency with the time-dependent integration. Naturally, more frequent Eddington tensor updates lead to a more accurate solution; in fact, Auer & Mihalas (1970) recommend iterating to convergence between the radiation and Eddington tensor fields. Unfortunately, this approach would be prohibitively time-consuming for our problem. Instead, we opt to update the Eddington tensor in a given computational cell only when the radiation field has changed significantly in that cell; this technique has been shown to be an excellent approximation in other contexts (for example, Hubeny & Burrows 2007). In particular, after each timestep, we re-compute the Eddington tensor in those cells where the photon number density has undergone a fractional change greater than  $f_{\mathcal{J}}$  in at least one frequency bin since the last update to its Eddington tensors. In order to determine how the resulting errors vary with  $f_{\mathcal{J}}$ , we compute the reionization of a static density field from  $z = 9 \rightarrow 6$  using  $f_{\mathcal{J}} = 0, 0.01, 0.05, 0.1, \text{ and } 0.5$ .

In Figure 8 we show how the resulting fractional errors vary with time. This figure demonstrates the power and flexibility of the moment method: even if we only compute the full angular dependence of the radiation field when it has changed by more than a factor of two ( $f_{\mathcal{J}} = 0.5$ ), the typical local errors are better than 20% at all times. Most importantly, because setting  $f_{\mathcal{J}} > 0$  results in less-frequent updates to the Eddington tensor field, it speeds up the computation considerably. Through direct testing, we find that the computation time  $t$  for our reionization calculation varies with  $f_{\mathcal{J}}$  as  $t \propto f_{\mathcal{J}}^{-0.5}$ .

We now examine the top panel of Figure 8 in more detail. At early times ( $x_{\text{HI}} > 0.5$ ), errors are small because reionization is dominated by the self-ionization of small, overdense regions rather than by radiation transport. Eddington tensor updates are frequent in overdense regions owing to the rapidly-evolving  $\mathcal{J}$ , but they are also fast because, in an optically thick universe, the  $\tau_{\text{max}}$  parameter insures that most of the LC line integrals terminate well before they arrive at the source. After  $x_{\text{HI}}$  drops below 0.5, the errors begin to grow. However, rather than growing without bound, they level off at a characteristic value that in turn grows with  $f_{\mathcal{J}}$ . This is the regime in which setting  $f_{\mathcal{J}} > 0$  yields the biggest savings in computation time because, on average, the LC line integrals traverse more cells before reaching  $\tau_{\text{max}}$ . On the other hand, the radiation field evolves more slowly because the rapidly-evolving overdense regions are already largely reionized. Hence setting  $f_{\mathcal{J}} > 0$  corresponds to culling the most expensive Eddington tensor updates aggressively while preserving the overall accuracy.

The bottom panel of Figure 8 indicates that the distribution of errors shifts to smaller errors with decreasing  $f_{\mathcal{J}}$ , with values of  $f_{\mathcal{J}}$  less than 0.1 leading to median errors  $\leq 10\%$ . In practice, errors may be slightly larger as the median error at a given timestep and  $f_{\mathcal{J}}$  increases slightly with increasing spatial resolution. Moreover, Figure 8 does not address errors in the topology of the ionization field, which may vary differently with  $f_{\mathcal{J}}$  (although McQuinn et al. 2007 argue that the topology of reionization is dominated by the emissivity field and  $x_{\text{HI}}$  and does not vary strongly with other parameters). The appropriate

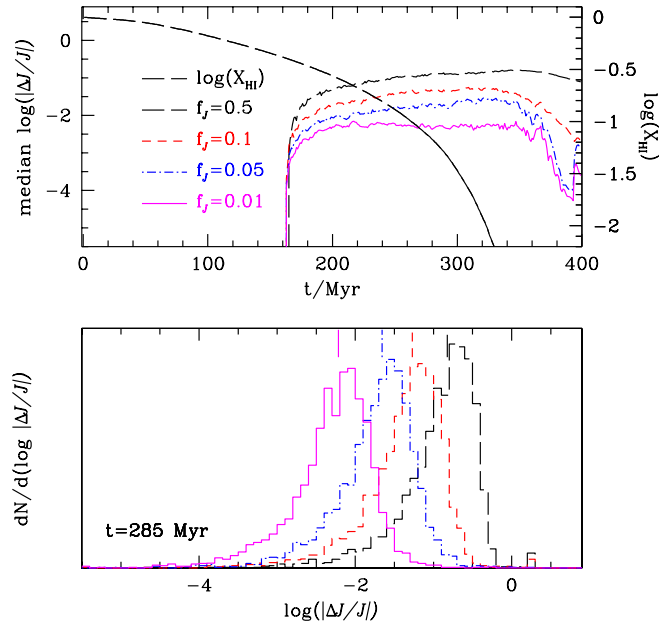


**Figure 8.** Convergence-testing the parameter that controls the frequency of updates to the Eddington tensor,  $f_{\mathcal{J}}$ , by comparing fractional errors in the local photon number density  $\mathcal{J}$  as a function of time. We compute reionization using  $f_{\mathcal{J}} = 0.5$  (black long-dashed),  $f_{\mathcal{J}} = 0.1$  (red short-dashed),  $f_{\mathcal{J}} = 0.05$  (blue dot-dashed) and  $f_{\mathcal{J}} = 0.01$  (magenta solid); the “converged” answer is obtained with  $f_{\mathcal{J}} = 0$ . The meanings of the various curves are analogous to Figure 6. Choosing  $f_{\mathcal{J}} = 0.05$  yields median errors better than 10% at all times.

choice of  $f_{\mathcal{J}}$ , therefore, depends on the problem. However, for reference, we note that choosing  $f_{\mathcal{J}} = 0.05$  generally leads to median errors that are better than 10% while speeding up the calculation by roughly a factor of three.

### 3.3.4 Full Error Budget

In Figure 9, we summarize the results of these convergence tests by comparing the distributions of errors in accuracy at  $t = 285$  that result from our fiducial choice of numerical parameters. The median errors for  $\tau_{\text{max}} = 6$ , hybrid  $n_d$ , and  $f_{\mathcal{J}} = 0.05$  are 8.0, 2.1, and 2.2%, respectively. Hence our fiducial choice of parameters leads to a typical numerical accuracy of 10% in  $\mathcal{J}$ .

## 3.4 Computational Scaling

The computation time for LC,  $t_{\text{LC}}$ , is proportional to the number of cells  $n_{\text{grid}}^3$ , the number of cells containing sources  $n_S$ , and the average length of a line integral in cells  $n_l$ :

$$t_{\text{LC}} \propto n_{\text{grid}}^3 n_S n_l$$

Both  $n_l$  and  $n_S$  generally vary with spatial resolution as well as with the mean opacity. In the limit of an optically thin volume ( $n_l \sim n_{\text{grid}}$ ) with nonzero emissivity everywhere ( $n_S = n_{\text{grid}}^3$ ),  $t_{\text{LC}} \propto n_{\text{grid}}^7$ , while in the limit of an optically thick medium ( $n_l$  constant) and highly clustered sources ( $n_S$  constant) the scaling flattens to  $t_{\text{LC}} \propto n_{\text{grid}}^3$ . Because  $t_{\text{LC}}$  potentially scales quite unfavorably with  $n_{\text{grid}}$ , we expect that it will ultimately dominate our spatial resolution limit. Hence, it is of interest to determine where the scaling falls for our problem. To do so, we gridded the same cosmological snapshot used in Section 3.3 onto grids of increasing spatial resolution assuming two different uniform ionized fractions,  $x_{\text{HI}} = 0.9$  and  $x_{\text{HI}} = 0.01$ . We then ran our LC code on these fields and used the gnu gprof utility to measure the computation time. We repeated the low-resolution tests up to ten times and averaged the results. For consistency, we set the periodic depth parameter to  $n_d = 1$  in all cases. We performed the calculations on a single 2-GHz AMD Athlon processor. In Figure 10 we compare the resulting scalings.

Looking at the nearly-neutral case ( $x_{\text{HI}} = 0.9$ ) first, we see that at coarse resolution our code scales as  $n_{\text{grid}}^{5.6}$ , indicating that  $n_S$  is increasing rapidly with increasing resolution. At higher resolutions the scaling flattens to  $n_{\text{grid}}^{3.4}$ , indicating both that  $n_S$  is varying only very slowly with resolution owing to source clustering and that  $n_l$  is varying more slowly than  $n_{\text{grid}}$  because most LC line integrals are terminated at the first cell owing to the high opacity.

Turning to the nearly-ionized case ( $x_{\text{HI}} = 0.01$ ), we find that the computation times are uniformly higher and the scaling is slightly steeper than in the nearly-neutral case, flattening from  $n_{\text{grid}}^{6.1}$  at coarse resolution to  $n_{\text{grid}}^{4.2}$  at high resolution. Because  $n_S$  is the same in both cases, these differences owe entirely to changes in  $n_l$ . First, in a more optically thin volume  $n_l$  is

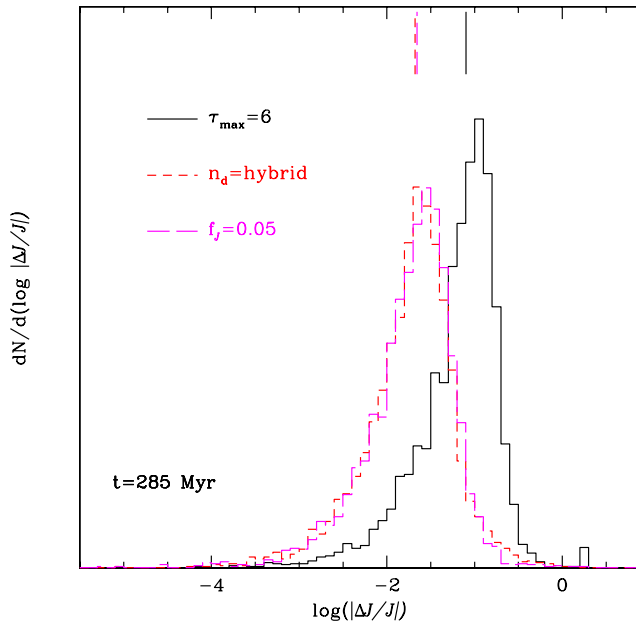


**Figure 9.** The distributions of accuracy error at  $t = 285$  for our fiducial choice of numerical parameters  $(\tau_{\max}, n_d, f_{\mathcal{J}}) = (6, \text{“hybrid”}, 0.05)$ . For this set of parameters, the error is dominated by the error owing to our choice of  $\tau_{\max}$ . Adding the median errors in quadrature, we expect a typical error of 9% in  $\mathcal{J}$ .

greater overall because, on average, line integrals traverse more cells before reaching  $\tau_{\max}$ . Second,  $n_l$  scales more nearly as  $n_{\text{grid}}$  because more of the line integrals proceed past the first cell even at low spatial resolution.

In summary, we find that, for the problem of cosmological reionization,  $t_{\text{LC}} \propto n_{\text{grid}}^{3.4-6.1}$ , depending on  $x_{\text{HI}}$  and  $n_{\text{grid}}$ . The flat scaling at high  $x_{\text{HI}}$  and high spatial resolution is encouraging, and indicates that LC should lend itself well to studying galaxy evolution well before the epoch of overlap ( $z = 6-7$ ). On the other hand, the generally longer computation times and steeper scaling at low  $x_{\text{HI}}$  indicate that our code will slow down considerably as the mean neutral fraction drops below 0.01. In future work we plan to study how to transition to the much faster optically thin approximation at this epoch without introducing significant inaccuracies.

#### 4 SOLVING FOR THE NON-EQUILIBRIUM IONIZATION STATES

In order to compute cosmological reionization, we must integrate the nonequilibrium equations for ionization and recombination of hydrogen and helium. A thorough discussion of the relevant chemical processes including analytic fits for the cross sections and reaction rates is provided by Anninos et al. (1997) and Abel et al. (1997). Here, we focus on deriving a technique for integrating these equations. We neglect  $\text{H}^-$  and  $\text{H}_2$  because we do not anticipate being able to resolve the mass scales at which these species are expected to dominate ( $< 10^8 M_{\odot}$ ; see, e.g., Couchman & Rees 1986). However, it would be trivial to extend our technique to account for these species as well.

Following Anninos et al. (1997), we write the equation that governs the abundance of species  $i$  schematically as

$$\frac{\partial n_i}{\partial t} = C_i(T, n_j) - D_i(T, n_j)n_i, \quad (16)$$

where  $C_i$  and  $D_i$  respectively represent source and destruction terms summed over all species  $j$  that can convert to or result from species  $i$ . Equation 16 can be modified to hold in an expanding universe by redefining  $n_i$  as the comoving number density and normalizing the reaction rate coefficients by  $a^3$ .

As is well known, Equation 16 can be quite stiff in the traditional sense; that is, its individual terms can evolve on very different timescales. This property has led many authors to adopt unconditionally stable integration techniques (see, e.g., Anninos et al. 1997; Mellema et al. 2006). Unfortunately, stable techniques are not necessarily accurate. Moreover, within cosmological density fields the timescales of the terms in Equation 16 can vary rapidly with position. For example, we have found that the timescales encountered during a typical reionization calculation at our expected spatial resolution can vary between  $10^{-4}$ – $10^2$  Myr at a given time. We have explored the stability and accuracy of a number of integration techniques when applied to a range of gas densities and ionization timescales in order to derive an optimal technique. Here we discuss two techniques, a fully implicit (FI) backwards differencing formula and second-order Runge-Kutta (RK2).

Backwards differencing Equation 16 results in the following difference equation for the updated density  $n_i^{n+1}$  in terms of

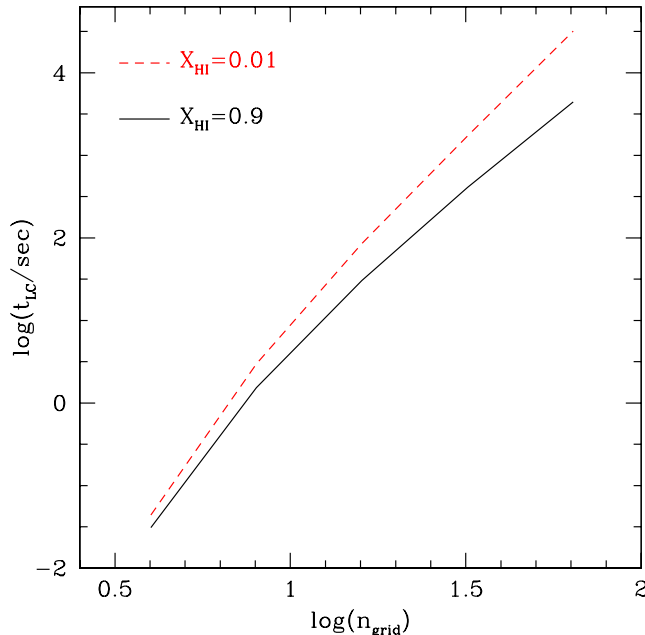


**Figure 10.** LC computation time versus number of grid cells to a side in the case of a mostly neutral (solid black) and highly ionized (dashed red) universe. The scaling flattens from  $n_{\text{grid}}^{5.6-6.1}$  at coarse resolution to  $n_{\text{grid}}^{3.4-4.2}$  at high resolution, depending on the neutral fraction  $x_{\text{HI}}$ .

the previous density  $n_i^n$  and the updated densities of the other species  $n_j^{n+1}$ :

$$\frac{n_i^{n+1} - n_i^n}{\Delta t} = C_i(T, n_j^{n+1}) - D_i(T, n_j^{n+1})n_i^{n+1}, \quad (17)$$

where all densities on the right hand side are evaluated at the updated time. This fully implicit technique is accurate to first order in time and is stiffly stable (Gear 1971). We solve the resulting set of algebraic equations using Newton-Raphson iteration. For 1 Myr timesteps, we have found that the iterative solution converges to within a tolerance of  $10^{-4}$  in fewer than 4 iterations, hence it is also reasonably efficient. However, evaluating and inverting the Jacobian is time-consuming. Moreover, in regimes where the shortest timescale is comparable to the timestep, its accuracy suffers because the rate coefficients at the end of the timestep are not a good approximation for their timestep-averaged values.

Second order explicit Runge-Kutta methods are accurate to second order in time and can be computed rapidly, but they become unstable if the timestep is comparable to or longer than the shortest relevant timescale. We have implemented the standard form of RK2 (e.g., Press et al. 1992). In addition, we have implemented a hybrid technique that combines the accuracy of RK2 around long timescales with the stability of implicit methods at short timescales. To do so, the hybrid technique simply checks all relevant timescales before each timestep and uses RK2 whenever the timestep is shorter than the shortest relevant timescale.

We test these techniques by solving Equation 16 for a single zone composed of pure hydrogen. The zone has a uniform, constant total number density and is initially entirely neutral. The ionizing radiation field is time-independent, and we refer to its intensity by its associated ionization timescale  $t_I$ . The relevant processes are radiative ionization, collisional ionization owing to collisions with electrons, and radiative recombination assuming case-B recombination rates. We evolve the ionization state using 0.5-Myr timesteps for 50 Myr and then determine the accumulated fractional error in the numerical result by comparing to the analytical solution. The total number density is  $1.66 \times 10^{-4} \text{ cm}^{-3}$ , roughly the cosmological mean density at  $z = 9$ , and we ignore Hubble expansion for simplicity.

In Figure 11 we compare the results of performing the test integration with our three schemes versus the analytical solution. In the top panel, we find that the accumulated fractional error varies nontrivially with  $t_I$ . For small  $t_I$  (i.e., intense ionizing backgrounds) the solution reaches ionization equilibrium well before the integration ends. In this “equilibrium regime” the error grows with decreasing  $t_I$ . We have found that the accuracy here cannot be further improved by integrating with smaller timesteps or switching to a higher-order finite-differencing scheme in time (for example, note that the second-order accurate RK2 scheme yields the same magnitude of error as the first-order accurate FI scheme for  $\log(t_I) = -0.5-1$ ). The “error floor” owes directly to roundoff error: if the machine accuracy is  $\epsilon_m$  and if the solution is close enough to equilibrium that the change in the next timestep is small compared to the current solution,  $|\dot{n}(n_i)|\Delta t < \epsilon_m n_i$ , then the error cannot decay.

For large enough  $t_I$  (weak ionizing backgrounds), the solution does not reach ionization equilibrium and roundoff error becomes subdominant. In this “nonequilibrium regime” the error is dominated by the usual truncation error in the finite-differencing scheme with the result that using shorter timesteps or switching to a higher-order finite differencing scheme

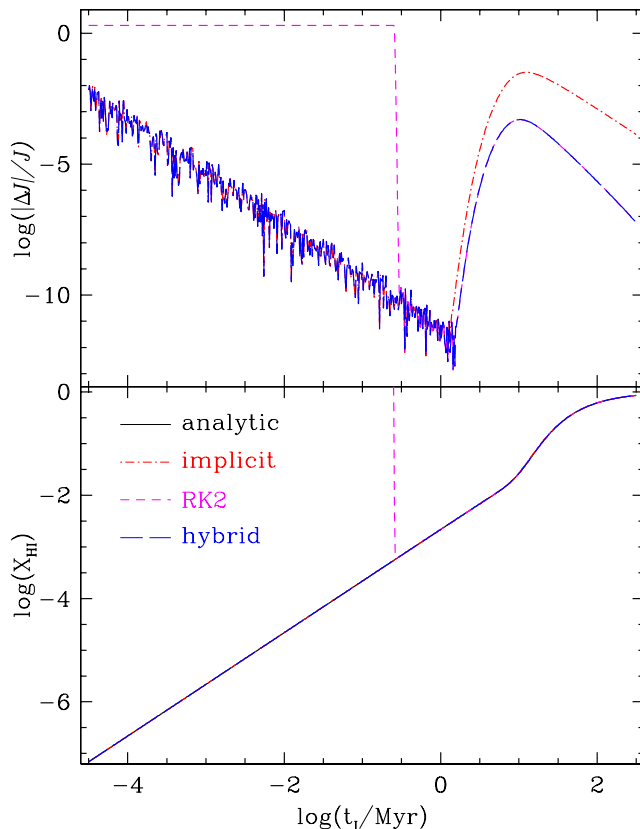


**Figure 11.** (top) Fractional error in final ionization state as a function of ionization timescale for three different nonequilibrium integration techniques. (bottom) Final neutral fraction for the same tests. For short ionization timescales the error is dominated by roundoff error while for long ionization timescales the accumulated error is dominated by timestep truncation error. A hybrid scheme using implicit differencing for short timescales and RK2 for long timescales is accurate to better than 1% in all regimes of interest.

improves the accuracy, as can immediately be seen from Figure 11. We repeated this test integration with a range of densities, timesteps, and integration times. In the nonequilibrium regime, we find that RK2 consistently yields accuracies better than 1% while FI often yields fractional errors of order unity.

To evaluate how much computation time we save through our hybrid technique, we tracked the number of calls to each of the two ionization routines throughout a test calculation of reionization similar to that in Section 6.3 but with only  $8^3$  computational cells. Before reionization ( $x_{\text{HI}} > 50\%$ ) RK2 is chosen 91% of the time, while after reionization it is chosen 38% of the time. Overall, RK2 is called 52% of the time. Noting that RK2 is  $\approx 4$  times faster than FI, our use of a hybrid technique rather than relying only on FI roughly halves the time required for evolving the ionization state. In other words, it simultaneously improves both the accuracy *and* the efficiency of our technique.

The bottom panel can be used to determine whether our tests span the domain of physical conditions that arise in cosmological calculations. At our anticipated spatial resolution ( $> 50h^{-1}\text{kpc}$ ),  $t_I$  ranges between  $10^{-4}$  and  $10^2$  Myr while the final (that is, post-recombination) hydrogen neutral fraction ranges between  $10^{-7}$  and 1. Our test calculations clearly span this domain, hence we conclude that our hybrid integration technique stably and efficiently yields fractional errors of  $\leq 1\%$  throughout our problem's domain.

## 5 PUTTING IT ALL TOGETHER

Having discussed our techniques for updating the Eddington tensor, radiation, and ionization fields, we now turn to our method for combining these ingredients into a single code. Figure 12 illustrates our algorithm for computing a single timestep. At the beginning, we solve self-consistently for the updated photon number densities  $\mathcal{J}^{n+1}$  and ionization states  $n^{n+1}$  in terms of the previous values ( $\mathcal{J}^n, \mathcal{F}^n, n^n$ ) through iteration. Schematically, we loop through the following calculations until the solutions have converged:

$$\begin{aligned} \mathcal{J}^{n+1} &= \mathcal{J}^{n+1}(\mathcal{J}^n, n^{n+1}, \mathcal{F}^n) \\ n^{n+1} &= n^{n+1}(\mathcal{J}^{n+1}, n^n) \end{aligned}$$

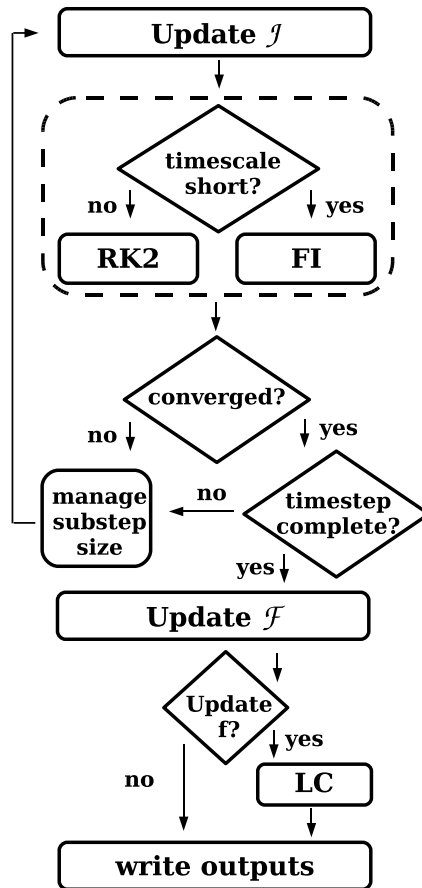


Figure 12. A single timestep in our code.

During the first iteration of each timestep, we use the values from the previous timestep as the initial guess for the updated values.

Because this scheme does not converge for general initial conditions and timestep  $\Delta t$ , we must include a treatment for reducing the timestep whenever necessary. We have implemented an adaptive stepsize scheme that is designed to collapse the timestep rapidly near difficult spots but then slowly accelerate as the integration grows smoother. In particular:

- (i) If the fractional error is less than  $10^{-4}$ , then we consider the solution to have converged. We halt the iteration and advance the timestep.
- (ii) If the fractional error does not reach  $10^{-4}$  in 15 iterations, we divide  $\Delta t$  by 4 and restart the iteration.
- (iii) If 4 consecutive substepped iterations converge, then we multiply  $\Delta t$  by 2.
- (iv) If the substepped timestep becomes smaller than  $10^{-5}$  of the original timestep, then we consider the computation to have diverged. In this case, we terminate the integration.

After updating the radiation and ionization fields, we compute the updated fluxes  $\mathcal{F}^{n+1}$ . We then compute the fractional change in each cell's  $\mathcal{J}$  since the last update to its Eddington tensor and update the Eddington tensors wherever the fractional change exceeds  $f_{\mathcal{J}}$ . This marks the end of a single timestep.

## 6 TESTS

### 6.1 Strömgren Spheres

We now demonstrate that our code accurately computes the growth of H II regions in both static and expanding media. For the static case, we locate a single O star of monochromatic ionizing luminosity  $5 \times 10^{48} \text{ s}^{-1}$  in a homogeneous medium of pure hydrogen with total density  $10^{-3} \text{ cm}^{-3}$ , temperature  $10^4 \text{ K}$ , and initial ionized fraction 0.0012 (Test 1 from Iliev et al. 2006). The simulation volume has a side length of 10.5 kpc and is divided into  $48^3$  cells. We evolve the nonequilibrium radiation and ionization fields for 500 Myr. In the bottom-left panel of Figure 13, we compare how the radius of the resulting ionization front grows with time in our code (solid) versus the exact analytical solution (dashed; Iliev et al. 2006). In the numerical case, we define the radius of the ionized region as the radius at which the neutral hydrogen fraction drops to 50%.

There is a slight tendency for the numerical radius to exceed the analytical one owing to the diffusive nature of the

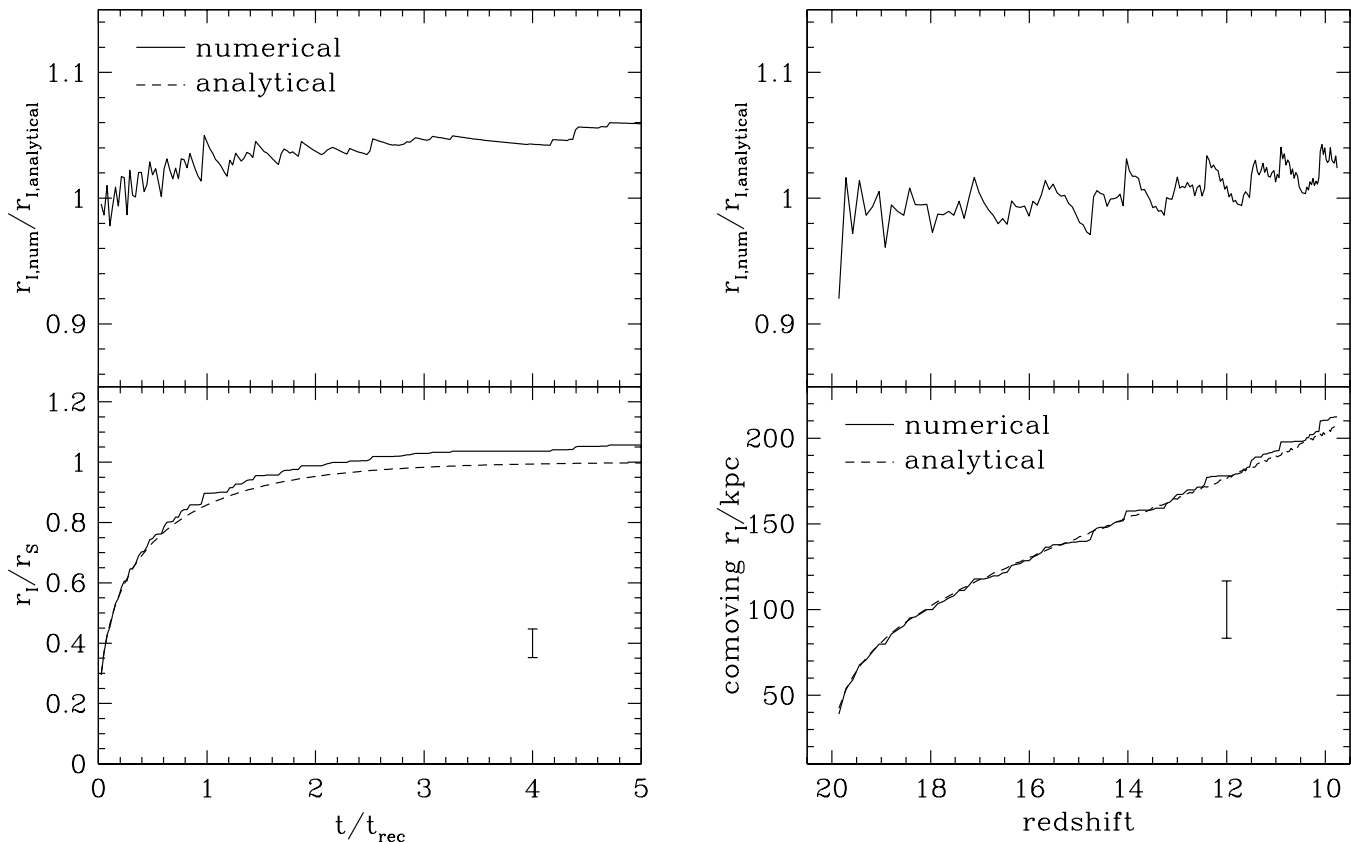


**Figure 13.** Test of classical (left) and cosmological (right) Strömgen spheres. In the bottom panels we show the numerical (solid) and analytical (dashed) solutions as a function of time. The error bars in the bottom panel are included for reference and span twice the width of a computational cell. In the top panels we show the ratio of the numerical to the analytical solutions. In both test cases, the numerical and analytical solutions agree to within one cell width at all times.

moment method (recall that the divergence in Equation 11 is computed from a 19-cell finite difference pattern). In order to put this effect into context, we include an error bar that spans twice the width of a single computational cell; this is our true spatial resolution. Comparing the error bar with the gap reveals that our method is accurate to within the uncertainty introduced by the finite spatial resolution. In the top panel we show the ratio of the numerical to the analytical solutions as a function of time. At all times, they agree to within 5%. Noting that the majority of the codes that are compared in Iliev et al. (2006) also yield ionization front radii that exceed the analytical solution by 1–5% (Figure 7 of Iliev et al. 2006), we conclude that our method’s accuracy is comparable to those codes.

For the expanding case, we consider a protogalaxy that “turns on” at  $z = 20$  with an ionizing luminosity  $5 \times 10^{49} \text{ s}^{-1}$  (this is roughly what is expected for  $10^4 M_\odot$  of young Population II stars assuming an ionizing escape fraction of 5%). The protogalaxy lives in a homogeneous medium of pure hydrogen with comoving density  $1.66 \times 10^{-7} \text{ cm}^{-3}$  and temperature  $10^4 \text{ K}$ . We evolve the test from  $z = 20 \rightarrow 10$  in an Einstein-de Sitter universe with  $h = 0.7$  using  $48^3$  computational cells. In the bottom right panel of Figure 13, we compare the comoving radius of the ionized region as a function of time in our numerical model (solid) against the analytical solution of Shapiro & Giroux (1987) (dashed). As before, the numerical solution tracks the analytical one to within the size of a grid cell at all times. In the top right panel we show the ratio of the numerical to the analytical solutions as a function of time. Once again, our numerical solution is accurate to within 5% at all times.

Combining the results of these tests, we conclude that our code conserves photons, accurately determines the nonequilibrium ionization states, and accounts for the relevant cosmological terms.

## 6.2 Shadowing

We now discuss how well our code is able to produce shadows. Our goal is to run a test case whose results can be compared to Test 3 of Iliev et al. (2006). However, this test involves irradiating a dense clump with a plane-parallel wavefront, a situation that is difficult to impose in our method. Instead, we consider the case of a dense clump of cold hydrogen irradiated by a bright disk located sufficiently far away that the flux from the disk at the clump is approximately plane-parallel. We calibrate the disk’s (isotropic) emissivity to the simulation resolution so that, if it were an infinite plane, the flux would be  $2 \times 10^6 \text{ s}^{-1}$

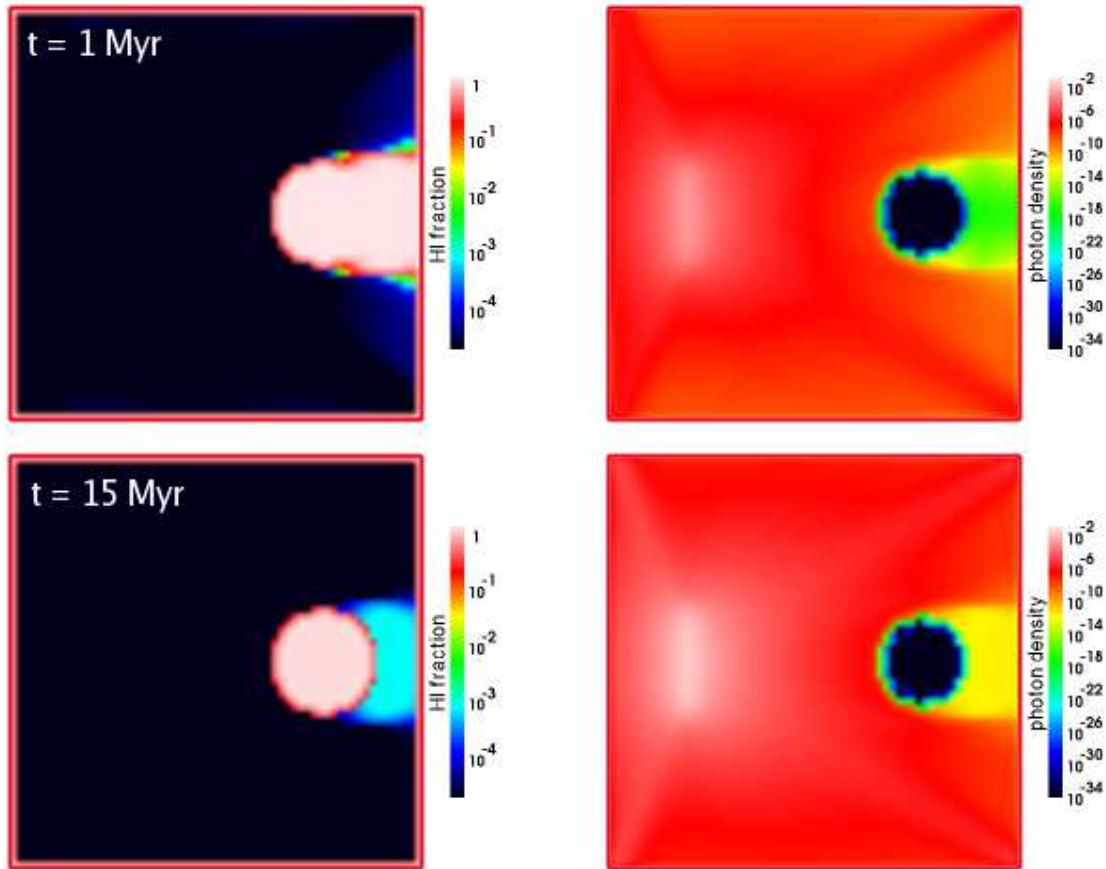


**Figure 14.** Test of ionization front trapping: a luminous disk irradiates a dense clump of the same radius in a diffuse medium. The left and right panels show the neutral hydrogen fraction and photon number density, respectively, in a plane cut through the middle of the simulation volume at  $t = 1$  (top) and 15 (bottom) Myr. The brightest areas give the position of the source, and the darkest areas give the position of the barrier. The “spokes” radiating from the source to the corners in the right panels are a numerical artifact of the opaque boundary with which we surround the simulation box in order to suppress periodic effects. Our moment method results in incomplete shadowing owing to numerical diffusion. These Figures were produced using IFRIT.

$\text{cm}^{-2}$ . The radius of the clump and the disk is 0.8 kpc, they are separated by 3.75 kpc, and the plane of the disk is oriented perpendicular to the line connecting the disk and the clump. The ambient hydrogen number density and temperature are  $2 \times 10^{-4} \text{ cm}^{-3}$  and 8000 K, while inside the clump they are  $0.04 \text{ cm}^{-3}$  and 40 K. The box size is 6.6 kpc and contains  $64^3$  computational cells. We evolve the simulation for 15 Myr.

Figure 14 shows the neutral hydrogen fraction and photon number density in the simulation mid-plane after 1 Myr (top panels) and 15 Myrs (bottom panels). In these figures the dense clump is on the right and the source disk, seen edge on, is on the left. Looking at the top panels first, we see that after 1 Myr the region behind the clump remains largely neutral although the rest of the volume is completely ionized, suggesting that our technique shadows well, with the photon density at this time 4–5 orders of magnitude fainter in the shadowed region than in the unshadowed one. The small amount of diffusion results from the fact that our LC module sets the Eddington tensors in the shadowed region to the isotropic case because no sources are visible there. Consequently, photons are free to diffuse into the shadowed region, as is expected in any moment formalism. After 15 Myr, the ionizing field behind the clump has strengthened to a photon number density of roughly 1% of the value in the unshadowed region, driving the neutral hydrogen fraction down to  $10^{-3}$ . At this point, the volume is in equilibrium; in fact, the radiation and ionization fields do not change appreciably between 5 and 15 Myr.

Comparing Figure 14 to Figures 22 and 24 of Iliev et al. (2006), we find that our technique shadows as well as ray-tracing and Monte Carlo codes at  $t = 1$  Myr. However, at  $t = 15$  Myr our code performs more poorly owing to the diffusion of photons into the shadowed region. Figure 14 can also be compared with Hayes & Norman (2003), who introduced a moment method that is similar to ours. They demonstrated that incorporating Eddington factors from a time-dependent short characteristics integration results in incomplete shadowing (see their Figures 6–9). They also found that increasing the spatial resolution did not resolve the problem. Instead, they concluded that the incomplete shadowing results from the fourth term in Equation 11, which involves the Laplacian of the product  $\mathbf{f}\mathcal{J}$ . Evaluating this term couples nonadjacent computational cells and gives rise to numerical diffusion in space. This might be expected to present even more of a problem in our technique given that we find

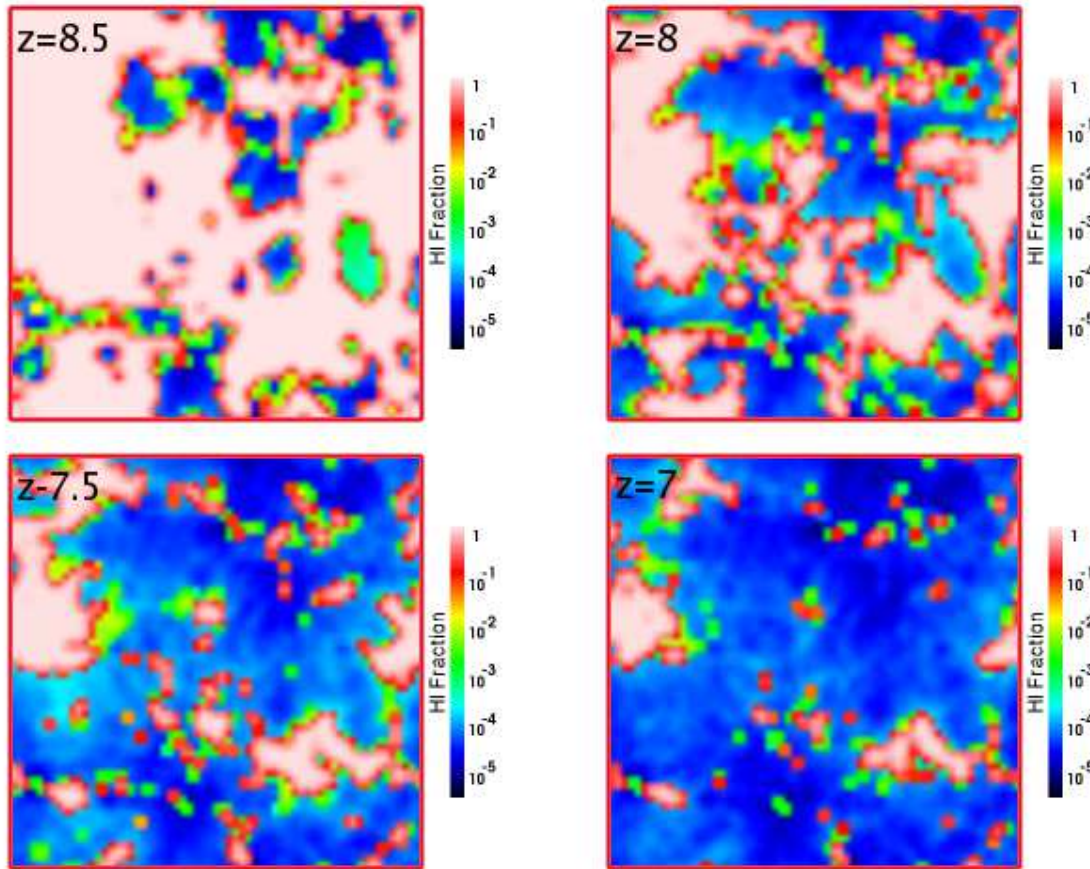


**Figure 15.** Two-dimensional slices through a reionization computation with a static emissivity field at four representative redshifts. The neutral hydrogen fractions are color-coded as indicated in the color bar and the redshifts are given in the top-left corner. These Figures were produced using IFRIT.

it necessary to smooth our Eddington tensors whereas they did not. Despite this, Figure 14 demonstrates that our technique can shadow quite effectively.

### 6.3 Cosmological Volume

For our final test, we compute the reionization of a cosmological density field in which we account for Hubble expansion but hold the emissivity and baryon density fields constant. We derive the initial conditions using the same output and the same gridding technique as in Section 3, but for this test we divide the volume into  $64^3$  rather than  $16^3$  computational cells so that each computational cell spans a comoving width of  $125h^{-1}\text{kpc}$ . Given that the parent simulation begins with  $256^3$  baryon particles, this implies that, on average, 64 baryon particles contribute to each cell, hence systematic errors associated with the gridding are dominated by effects related to low spatial resolution rather than to Poisson statistics. We do not attempt a detailed treatment of subgrid physics as our focus is on our radiative transfer technique (for a careful treatment of these issues see McQuinn et al. 2007). We evolve the ionization and radiation fields from  $z = 9 \rightarrow 6$  with outputs spaced 1 Myr apart assuming  $(\Omega, \Lambda, H_0) = (0.3, 0.7, 70)$ . We set  $n_d = 1$  and update the full Eddington tensor field whenever the photon number density has changed by more than a factor of two in at least 20% of the volume, and after  $x_{\text{HI}}$  drops below 0.5% we use the optically thin approximation (tests indicate that this yields better than 20% accuracy in  $\mathcal{J}$ ). This computation required roughly 10000 CPU hours using 32 1.6 GHz Itanium2 processors in a shared-memory environment. Note that, although this test computation is only intended as a proof-of-concept for our method, it is already quite realistic in the sense that the gas density and emissivity fields derive from a cosmological hydrodynamic simulation that simultaneously reproduces a wide array of observations of galaxies (Davé et al. 2006; Bouwens et al. 2007; Finlator & Davé 2008) and the intergalactic medium (Oppenheimer & Davé 2006) in the post-reionization universe.

In Figure 15, we show the neutral fraction as a function of position in a two-dimensional slice through the computational volume at four representative redshifts. Reionization proceeds in the familiar way: At early times, individual ionized bubbles grow around the brightest sources, which are strongly clustered. As reionization proceeds, the individual ionized regions begin to overlap; this process can be seen to be well underway by  $z = 8$ . The volume-averaged neutral hydrogen fraction dips below 50% at  $z \approx 7.75$ . Around this time, the mean free path of ionizing photons grows comparable to the length of the simulation

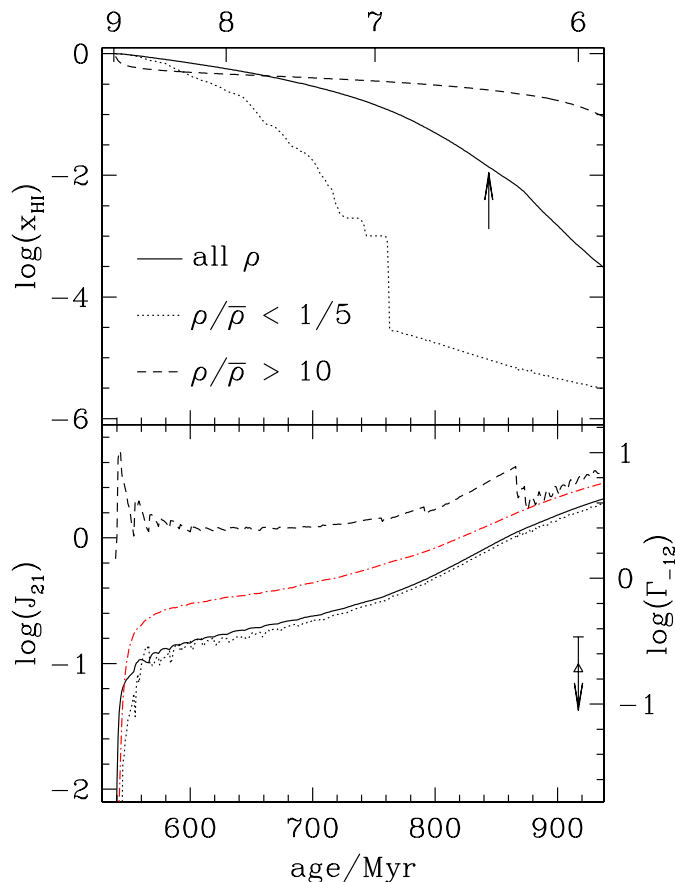


**Figure 16.** Volume-averaged neutral hydrogen fraction (top) and the ionizing background mean intensity  $J_{21}$  (bottom) as a function of the age of the Universe (bottom axis) and redshift (top axis). The right axis in the bottom panel indicates the hydrogen ionization rate in units of  $10^{-12} \text{ s}^{-1}$ . In both panels, the solid line is the average over all space whereas the dotted and dashed lines are averaged over underdense and overdense regions, respectively. The red dot-dashed curve in the bottom panel shows how the volume-averaged  $J_{21}$  varies at half our spatial resolution. The arrow in the top panel indicates the observed limit on  $x_{\text{HI}}$  at  $z = 6.4$  (Fan et al. 2006), while the limit in the bottom panel is representative of observed limits on the ionization rate at  $z = 6$  (Bolton & Haehnelt 2007).

volume and the ionization field becomes a network of simply-connected regions that are largely ionized and isolated regions that are largely neutral. As this topology emerges, the ionizing background continues to strengthen and the remaining neutral regions continue to shrink. Finally, in the post-overlap universe only regions with high recombination rates and low emissivities remain neutral.

In Figure 16, we give a more quantitative view of how reionization proceeds in our calculation. In the top panel, we compare the neutral hydrogen fraction  $x_{\text{HI}}$  averaged over the entire computational volume with the average over underdense and overdense regions. At the beginning of our computation, overdense regions are more rapidly ionized because they host the bulk of the ionizing sources. Meanwhile, underdense regions remain more neutral because they have not yet been penetrated by ionization fronts. As reionization proceeds, ionization fronts begin propagating into underdense regions, which rapidly become more highly ionized than the overdense regions.  $x_{\text{HI}}$  continues to shrink in all three density bins until  $z \sim 6$ , by which point most of the universe has arrived at ionization equilibrium with a fairly uniform ionizing background. At this time  $x_{\text{HI}}$  has dropped to  $x_{\text{HI}} \sim 10^{-3}$ , in good agreement with observations (Fan et al. 2006).

We show how the relation between density and ionization fraction evolves in a different way in Figure 17. Here, the different curves show the median relation at five representative ionization fractions as indicated. At early times, highly overdense regions ionize to a neutral fraction below  $< 10^{-4}$  even when the cosmological mean neutral fraction remains at 99% owing to their high emissivities. Regions that are at and below the mean density ionize next owing to their low recombination rates. Mildly overdense regions ionize last owing to their blend of relatively high recombination rates and low emissivities.

The reversal in the trend of ionization fraction versus overdensity that we find at  $z \sim 8$  has recently been discussed in the semi-numerical study of Choudhury et al. (2008). In this work, it is argued that underdense regions should be more strongly ionized than overdense regions at late stages in reionization owing to their lower recombination rates. Our test computation, which (automatically) treats recombination rates realistically, supports their results while making far fewer assumptions regarding baryonic physics. Unfortunately, our test cannot be used to study the most overdense regions before

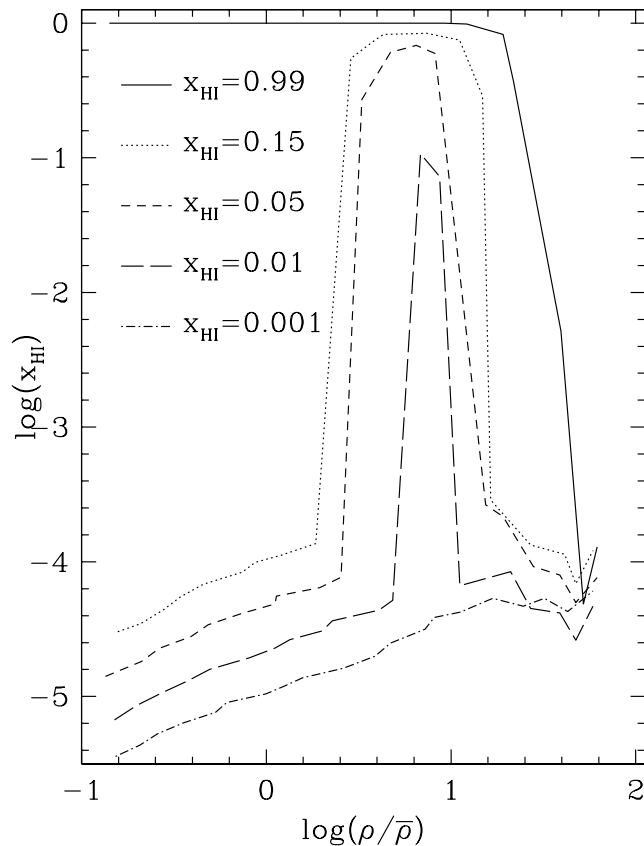


**Figure 17.** Median neutral fraction as a function of normalized density at five Hydrogen neutral fractions as indicated. The curves correspond to redshifts of (top to bottom) 8.9, 7.0, 6.7, 6.3, and 6.0 in our simulation.

$z \approx 8$  owing to the spatial resolution of this particular simulation; this point will become clear when we examine the bottom panel of Figure 16.

In the bottom panel of Figure 16, we compare the time evolution of the volume-averaged mean specific intensity at the Lyman limit  $J_{21} \equiv J_\nu(\nu_H)$  for the same bins of density. We estimate  $J_{21}$  following Mesinger & Dijkstra (2008) by assuming that the ionizing photons are distributed as a power law of the form  $J(\nu) = J_{21}(\nu/\nu_H)^{-\alpha} \times 10^{-21} \text{ erg s}^{-1} \text{ Hz}^{-1} \text{ cm}^{-2} \text{ sr}^{-1}$  with  $\alpha = 4.7$ , which is appropriate for the typical age and metallicity of stars at  $z = 9$  in our simulations. Throughout reionization, overdense regions see a more intense ionizing background than the volume average. As we saw in the top panel, this leads them to reionize first. Unfortunately, this computation does not resolve reionization around the most overdense cells at  $z > 8$  because, in these regions,  $J_{21}$  is not smooth enough spatially. The strong peaks in  $J_{21}$  around the brightest sources lead to inaccurately computed fluxes, which in turn lead to overestimates in  $J_{21}$ . After  $z = 8$ , however, the HII regions around these cells grow and  $J_{21}$  becomes smoother and consequently more accurate. By contrast, the ionizing background in underdense regions tracks the volume average at all times, supporting the idea that underdense regions remain more highly ionized at late times owing to their lower recombination rates rather than a stronger  $J_{21}$ .

The right axis converts  $J_{21}$  into its associated hydrogen ionization rate  $\Gamma_{-12} \equiv \Gamma_{\text{HI}}/10^{-12}$ . The open triangle indicates the observed upper limit on  $\Gamma_{-12}$  at  $z = 6$  from Bolton & Haehnelt (2007). The arrow's length combines the uncertainties in cosmology, the observed Lyman- $\alpha$  forest effective optical depths used to derive  $\Gamma_{-12}$ , and the thermal state of the intergalactic medium. This observation is representative of other constraints from the literature. Comparing the Bolton & Haehnelt (2007) constraint against our simulation suggests that the simulated  $\Gamma_{-12}$  is a factor of  $\sim 20$  too high. This is surprising for several reasons. First, our emissivity field corresponds to the galaxy population at  $z = 9$  and does not account for the rise in the star formation rate density that occurs between  $z = 9$  and  $z = 6$  (Oppenheimer & Davé 2006). Second, we assume an ionizing escape fraction of 10%, whereas Bolton & Haehnelt (2007) suggest that an escape fraction of up to 20% may be required in order to maintain the observed ionization state of the intergalactic medium at  $z = 6$ . Third, we start our test at  $z = 9$  whereas observations from WMAP-5 are best fit by an instantaneous reionization redshift of  $11.0 \pm 1.4$  (Dunkley et al. 2008), which suggests that reionization was already well underway by  $z = 9$ . Finally, we do not include active galactic nuclei. All of our assumptions, therefore, tend to *underestimate* the value of  $\Gamma_{-12}$ . The source of the discrepancy could lie in cosmic variance, low spatial resolution, or the uncertainty in the choice of ionizing escape fraction. As a quick test, we have plotted the evolution of  $J_{21}$  in a separate test in which the same density field was divided into  $32^3$  rather than  $64^3$  cells (red dot-dashed

curve). The resulting curve suggests that some, but not all, of the discrepancy owes to poor spatial resolution. However, further investigation into this discrepancy is beyond the scope of this work.

## 7 SUMMARY

In this paper, we introduced a method that accurately and efficiently computes continuum radiative transfer in static density fields. The code uses a moment-based approach to solve the equation of comoving radiative transfer, with the Eddington tensors obtained using a long characteristics method. We compared several techniques for computing the Eddington tensors that are needed to close the moment hierarchy and demonstrated that, of the three methods that we investigated, only the method of long characteristics has the ability to compute highly inhomogeneous radiation fields without introducing numerical artifacts. We found through direct measurement that the computation times for our long characteristics and moments modules scale with the number of computational cells  $N_{\text{cells}}$  as  $N_{\text{cells}}^{1.5}$  and  $N_{\text{cells}}^{1.0}$ , respectively. Next, we introduced a hybrid method for computing the evolution of nonequilibrium ionization fields and demonstrated that it is accurate to 1% throughout our computational domain. We combined this with our radiative transfer code via an efficient iterative algorithm. The final code is regulated by a number of parameters, and we characterized how these parameters impact computation time and accuracy using a suite of low-resolution convergence tests.

We subjected our method to a number of standard problems in continuum radiative transfer. First, we verified that our code accurately computes the growth of an H II region about a source in the classical (static) case as well as in the case of an expanding medium. We found that, in both cases, the radius of the resulting ionized region agrees with analytic expectations to within the computation’s spatial resolution at all times. Next, we tested whether our code is able to produce shadows behind opaque regions. In agreement with previous work, we found that the moment method introduces a small diffusion into the shadowed region (Hayes & Norman 2003). Nevertheless, we found that the strength of the radiation field in the shadowed region was up to only 1% of the value in the unshadowed region. Finally, we computed the reionization of an expanding cosmological volume and found qualitative agreement with other work in the literature.

Our code currently accounts for radiative and collisional ionization of hydrogen and helium as well as radiative recombination. It does not account for recombination radiation. Additionally, it does not follow the evolution of the temperature field, hence it does not account for photoionization suppression of star formation in low-mass halos, photoionization heating, recombination cooling, or shock formation.

In the future we plan to expand on our code in several ways. First, we have found that the computation time increases dramatically as the universe becomes optically thin because the LC line integrals traverse more cells before terminating either because they arrive at the source or because they reach  $\tau_{\text{max}}$ . However, in this regime, the optically-thin approximation, which is roughly ten times faster than LC, becomes increasingly valid. For this reason, we plan to study how to transition smoothly from LC to the optically thin approximation without introducing accuracy errors. Second, we will generalize our method to multifrequency radiative transfer, which is necessary for studying, for example, ionization front hardening or He II reionization. Finally, we plan to merge our radiative transfer scheme with our version of the cosmological galaxy formation code GADGET-2.

## ACKNOWLEDGEMENTS

We thank Dimitrios Psaltis, Philip Pinto, Marc Metchnik, Daniel Eisenstein, Ivan Hubeny, Moysey Brio, Rainer Wehrse, and Ben Oppenheimer for assistance and useful discussions. We thank Nick Gnedin for making his excellent visualization package IFRIT publically available. Our cosmological hydrodynamic simulation was run on the Xeon Linux Supercluster at the National Center for Supercomputing Applications, and many of our radiative transfer computations were run on the University of Arizona’s SGI Altix 4700 computer “Marin.” KF acknowledges support from a National Science Foundation Graduate Research Fellowship. FÖ acknowledges support from NSF grant AST 07-08640. Support for this work was provided by the NASA Astrophysics Theory Program through grant NNG06GH98G, as well as through grant number HST-AR-10647 from the SPACE TELESCOPE SCIENCE INSTITUTE, which is operated by AURA, Inc. under NASA contract NAS5-26555. Support for this work, part of the Spitzer Space Telescope Theoretical Research Program, was also provided by NASA through a contract issued by the Jet Propulsion Laboratory, California Institute of Technology under a contract with NASA.

**REFERENCES**

- Abel, T., Wise, J. H., & Bryan, G. L. 2007, *ApJL*, 659, L87
- Abel, T., & Wandelt, B. D. 2002, *MNRAS*, 330, L53
- Abel, T., Anninos, P., Zhang, Y., & Norman, M. L. 1997, *New Astronomy*, 2, 181
- Abel, T., Norman, M. L., & Madau, P. 1999, *ApJ*, 523, 66
- Anninos, P., Zhang, Y., Abel, T., & Norman, M. L. 1997, *New Astronomy*, 2, 209
- Auer, L. H., & Mihalas, D. 1970, *MNRAS*, 149, 65
- Bolton, J. S., & Haehnelt, M. G. 2007, *MNRAS*, 382, 325
- Bouwens, R. J., Illingworth, G. D., Blakeslee, J. P., & Franx, M. 2006, *ApJ*, 653, 53
- Bouwens, R. J., Illingworth, G. D., Franx, M., & Ford, H. 2007, *ApJ*, 670, 928
- Bruzual, G. & Charlot, S. 2003, *MNRAS*, 344, 1000
- Cen, R. 2002, *ApJS*, 141, 211
- Choudhury, T. R., Haehnelt, M. G., & Regan, J. 2008, *ArXiv e-prints*, 806, arXiv:0806.1524
- Ciardi, B., Ferrara, A., Governato, F., & Jenkins, A. 2000, *MNRAS*, 314, 611
- Ciardi, B., Ferrara, A., Marri, S., & Raimondo, G. 2001, *MNRAS*, 324, 381
- Couchman, H. M. P., & Rees, M. J. 1986, *MNRAS*, 221, 53
- Davé, R., Finlator, K., & Oppenheimer, B. D. 2006, *MNRAS*, 370, 273
- Dunkley, J., et al. 2008, *ArXiv e-prints*, 803, arXiv:0803.0586
- Fan, X., et al. 2006, *AJ*, 132, 117
- Fan, X. 2007, *Cosmic Frontiers*, 379, 35
- Finlator, K., Davé, R., & Oppenheimer, B. D. 2007, *MNRAS*, 376, 1861
- Finlator, K., & Davé, R. 2008, *MNRAS*, 385, 2181
- Furlanetto, S. R., Zaldarriaga, M., & Hernquist, L. 2004, *ApJ*, 613, 1
- Numerical Initial Value Problems in Ordinary Differential Equations, Prentice-Hall, Englewood Cliffs, New Jersey
- Geil, P. M., & Wyithe, J. S. B. 2008, *MNRAS*, 386, 1683
- Gnedin, N. Y., & Ostriker, J. P. 1997, *ApJ*, 486, 581
- Gnedin, N. Y., & Abel, T. 2001, *New Astronomy*, 6, 437
- Hayes, J. C., & Norman, M. L. 2003, *ApJS*, 147, 197
- Hayes, J. C., Norman, M. L., Fiedler, R. A., Bordner, J. O., Li, P. S., Clark, S. E., ud-Doula, A., & Mac Low, M.-M. 2006, *ApJS*, 165, 188
- Hubeny, I., & Burrows, A. 2007, *ApJ*, 659, 1458
- Iliev, I. T., Scannapieco, E., & Shapiro, P. R. 2005, *ApJ*, 624, 491
- Iliev, I. T., et al. 2006, *MNRAS*, 371, 1057
- Iliev, I. T., Mellema, G., Shapiro, P. R., & Pen, U.-L. 2007, *MNRAS*, 376, 534
- Iliev, I. T., Shapiro, P. R., McDonald, P., Mellema, G., & Pen, U.-L. 2007, *ArXiv e-prints*, 711, arXiv:0711.2944
- Kunasz, P., & Auer, L. H. 1988, *Journal of Quantitative Spectroscopy and Radiative Transfer*, 39, 67
- Kramer, R. H., Haiman, Z., & Oh, S. P. 2006, *ApJ*, 649, 570
- Madau, P., Haardt, F., & Rees, M. J. 1999, *ApJ*, 514, 648
- Mellema, G., Iliev, I. T., Alvarez, M. A., & Shapiro, P. R. 2006, *New Astronomy*, 11, 374
- Mesinger, A., & Dijkstra, M. 2008, *ArXiv e-prints*, 806, arXiv:0806.3090
- Mesinger, A., & Furlanetto, S. 2007, *ApJ*, 669, 663
- Mihalas, D. M., & Weaver, R. P. 1982, *Journal of Quantitative Spectroscopy and Radiative Transfer*, 28, 213
- McQuinn, M., Lidz, A., Zahn, O., Dutta, S., Hernquist, L., & Zaldarriaga, M. 2007, *MNRAS*, 377, 1043
- Oppenheimer, B. D., & Davé, R. 2006, *MNRAS*, 373, 1265
- Press, W. H., Teukolsky, S. A., Vetterling, W. T., & Flannery, B. P. 1992, *Numerical Recipes in C: The Art of Scientific Computing* (New York, NY: Cambridge University Press)
- Razoumov, A. O., & Scott, D. 1999, *MNRAS*, 309, 287
- Rijkhorst, E.-J., Plewa, T., Dubey, A., & Mellema, G. 2006, *A&A*, 452, 907
- Shapiro, P. R., & Giroux, M. L. 1987, *ApJL*, 321, L107
- Sokasian, A., Abel, T., & Hernquist, L. E. 2001, *New Astronomy*, 6, 359
- Spergel, D. N., et al. 2007, *ApJS*, 170, 377
- Stone, J. M., Mihalas, D., & Norman, M. L. 1992, *ApJS*, 80, 819
- Wyithe, J. S. B., & Loeb, A. 2003, *ApJ*, 586, 693